Time-dependent dike propagation from joint inversion of seismicity and deformation data

P. Segall,[1] A. L. Llenos,[1,2] S.-H. Yun,[3] A. M. Bradley,[1] and E. M. Syracuse[4,5]

[1]   Dike intrusions both deform Earth's surface and induce propagating earthquake swarms. We develop methods to utilize both deformation and seismicity from brittle, volcano-tectonic earthquakes to image time-dependent dike propagation. Dieterich's (1994) seismicity-rate theory is used to relate dike-induced stress changes to seismicity rate and is combined with elastic Green's functions relating dike opening to deformation. Different space-time patterns of seismicity develop if earthquakes occur at the same depth as the dike compared to above/below the dike. In the former, seismicity initiates near the dike's leading edges but shuts off as the dike tips pass and seismogenic volumes fall into stress shadows. In the latter, seismicity continues at a decaying rate after the tips pass. We focus on lateral propagation and develop a nonlinear inversion method that estimates dike length and pressure as a function of time. The method is applied to the 2007 Father's Day intrusion in Kilauea Volcano. Seismicity is concentrated at ~ 3 km depth, comparable to geodetic estimates of dike depth, and decays rapidly in time. With lateral propagation only and a vertical dike-tip line, it is difficult to fit both GPS data and the rapid down-rift jump in seismicity, suggesting significant vertical propagation. For the events to have occurred below the dike requires a very short aftershock decay time, hence unreasonably high background stressing rate. The rapid decay is better explained if the dike extends somewhat below the seismicity. We suggest that joint inversion is useful for studying the diking process and may allow for improved short-term eruption forecasts.

1. Introduction

[2]   Seismicity and ground deformation are the two most important geophysical methods for monitoring volcanoes. Yet, these data are essentially never combined in a quantitative manner for monitoring purposes. We suggest that a rigorous method for jointly analyzing seismic and deformation data could lead to improved eruption forecasts. Because the geometry of dikes is relatively well defined by both geologic and geophysical observations, they offer the most promising target for joint deformation and seismic analysis. Dike intrusions cause stress changes and thus not only deform the Earth's surface but also commonly induce propagating swarms of earthquakes. In this paper we develop a method that utilizes seismicity and geodetic data in a joint inversion to model dike propagation. The inversion provides time-dependent estimates of dike geometry and excess magma pressure (magma pressure in excess of the dike normal compressive stress). Equally importantly, the inversion methodology allows us to test competing models for dike-induced earthquakes by examining goodness of fit to both geodetic and seismic observations.

[3]   We begin by reviewing observations from a number of volcanic settings. Earthquake swarms in Kilauea volcano's rift zones are common. Swarms typically propagate down-rift, away from Kilauea's summit into either the East Rift Zone (ERZ) or southwest rift zone (SWRZ), with the leading edge of seismicity advancing at rates of 0.1 to 6 km/h [*Klein et al.*, 1987]. As an example, Figure 1 summarizes deformation and seismicity during the June 2007 "Father's Day" intrusion and eruption in Kilauea's ERZ. The intrusion began on 17 June 2007 accompanied by an earthquake swarm that lasted almost 3 days, during which seismicity propagated down-rift, away from the summit caldera. Ultimately, a small volume of basalt erupted at the distal end of the earthquake swarm. During the intrusion Global Positioning System (GPS) stations and tiltmeters recorded steadily increasing deformation adjacent to the rift zone. The Father's Day intrusion is discussed in more detail in section 4.

[1]Department of Geophysics, Stanford University, Stanford, California, USA.
[2]Now at Earthquake Science Center, US Geological Survey, Menlo Park, California, USA.
[3]Jet Propulsion Laboratory, California Institute of Technology, Pasadena, California, USA.
[4]Department of Geoscience, University of Wisconsin, Madison, Wisconsin, USA.
[5]Now at Los Alamos National Laboratory, Los Alamos, New Mexico, USA.

Corresponding author: P. Segall, Department of Geophysics, Stanford University, Mitchell Bldg., 397 Panama Mall, Stanford, CA 94305-2215, USA. (segall@stanford.edu)
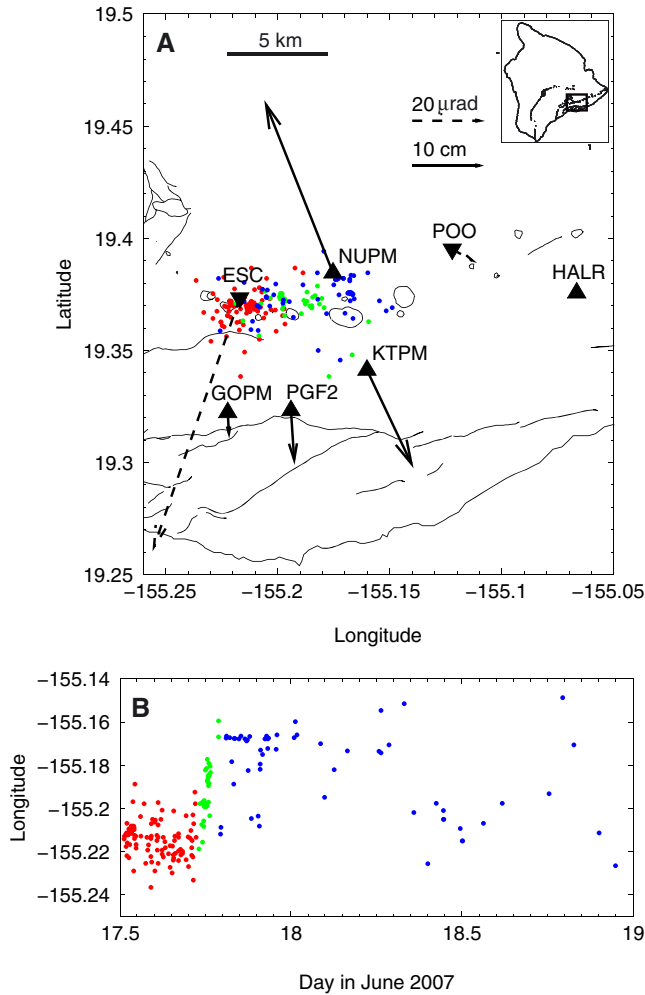
Figure 1. (a) Map showing the island of Hawaii (inset) and Kilauea's East Rift Zone. Dots indicate relocated earthquakes (color indicates timing according to the intrusion chronology of *Poland et al.* [2008], with red between days 17.51 and 17.73, green between days 17.73 and 17.79, and blue between days 17.79 and 18.7). Vectors indicate cumulative observed displacement and tilt (dashed). (b) Space-time evolution of the seismicity during the intrusion.

[4] Accurate earthquake locations derived using waveform cross correlation during the 1983 intrusion that initiated the ongoing Pu'u 'Ō'ō eruption reveal an extremely narrow 16 km long zone at a depth of 3–4 km within the ERZ [*Rubin et al.*, 1998]. The leading edge of seismicity extended down-rift at a rate of ∼ 0.7 km/h. The swarm was accompanied by a sequence of tilt changes consistent with a laterally propagating opening dislocation [*Okamura et al.*, 1988]. These observations confirm that deformation and seismicity represent different responses to the same underlying physical process. Geodetic observations in 1983 provide limited constraint on the depth of intrusion but are generally consistent with dike opening from near Earth's surface to a depth of 3.0 to 4.5 km [*Wallace and Delaney*, 1995]. Subsequent intrusions in the middle ERZ captured by GPS and more recently interferometric synthetic aperture radar (InSAR) observations in 1997, 1999, and 2007 extended to

depths of roughly 2.5 ± 1 km [*Owen et al.*, 2000a; *Cervelli et al.*, 2002; *Montgomery-Brown et al.*, 2010]. In summary, within considerable uncertainties the depths of the 1983 swarm earthquakes are consistent with the bottoms of ERZ dike intrusions inferred from geodetic data.

[5] The most obvious explanation for the narrow depth extent of dike-induced earthquakes on Kilauea is that the seismicity is controlled by strong stress concentrations at the dike bottoms. This view is supported by the general agreement between the geodetically inferred depth extent of dike opening and the depth of swarm seismicity. However, if the depth extent of diking is controlled by a temperature-dependent brittle-ductile transition, such that dikes extend partially into deeper ductile rock, the background deviatoric stresses at dike bottoms may be insufficient to generate earthquakes [*Rubin et al.*, 1998]. In this case the narrow depth extent of seismicity could be controlled by strong stress concentrations at the top of a deep rift body, which is estimated to occur at ∼ 3 km depth [*Delaney et al.*, 1990; *Owen et al.*, 2000b]. These effects are not independent; it is likely that both the top of deep rift opening and the bottom of episodic dike intrusions are ultimately controlled by a temperature-dependent rheological transition and associated background stress distributions. Thus, the stress concentrations due to diking as well as deep rift opening are likely to occur at comparable depths.

[6] One objective, then, is to contrast models in which the triggered earthquakes occur below the dike bottom from models in which earthquakes occur adjacent to the dike but near its bottom. Existing geodetic data alone cannot distinguish between these models. However, the stress fields are sensitive to the relative location of the dike bottom (Figure 2). If the earthquakes occur in the crust adjacent to the dike but above its lower tip line, the stress will first increase as the dike-tip stress concentration approaches but then decrease as the source volume enters a stress shadow.
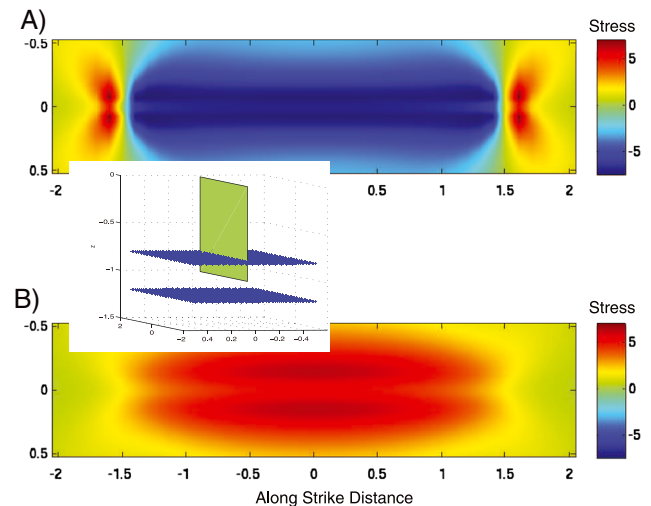
Figure 2. Coulomb stress resolved on optimally oriented strike-slip faults at two depths relative to the dike: (a) above the dike bottom (80% of the dike depth), and (b) below the dike bottom (120% of the dike depth). Inset shows geometry of the two horizontal image surfaces (blue) relative to the dike (green).
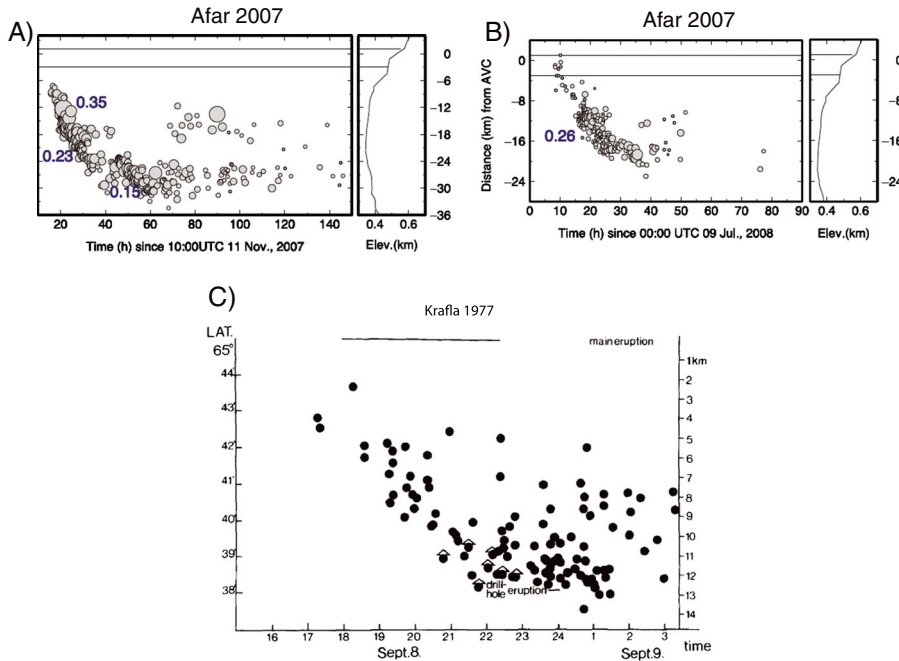
Figure 3. Space-time distribution of seismicity associated with intrusions in Afar and Iceland. (a) The November 2007 sequence along the Dabbahu-Manda-Hararo rift segment in Ethiopia. (b) July 2008 sequence; numbers indicate average propagation rates in m/s, after *Belachew et al.* [2011]. (c) The 1977 Krafla sequence, after *Brandsdottir and Einarsson* [1979]. Epicenters with location errors less than 2 km are plotted; triangles mark events with $M \geq 3$.

This is different for volumes of rock below the lower tip line, which always experience a positive stress change. As illustrated below, there is thus a marked difference in the space-time evolution of seismicity in these two cases. Thus, there is the potential for the seismicity to distinguish between the two models. In either case, dikes in Kilauea's ERZ almost certainly propagate into a strongly depth-varying background stress field generated by flank motion and deep rift opening. This is reflected in the depth distribution of background seismicity which is strongly localized at ~ 3 km [*Rubin et al.*, 1998; *Syracuse et al.*, 2010].

[7] Propagating earthquake swarms have also been well documented in other regions including Japan, Iceland, and the East Africa rift. The 2000 Miyakejima, Japan, swarm was particularly energetic with more than 7000 $M \geq 3$ shocks over a period of nearly 2 months. The Miyake-jima swarm extended laterally over a weeklong period and was accompanied by substantial displacements measured by GPS on nearby islands [*Toda et al.*, 2002]. In the past decade there have been more than a dozen dike injections in the Afar region of Ethiopia accompanied by earthquake swarms (Figures 3a and 3b) that propagated at rates of the order of 1 km/h [*Ebinger et al.*, 2010; *Belachew et al.*, 2011; *Grandin et al.*, 2011]. These intrusions have also been recorded by InSAR and GPS measurements.

[8] In most cases the dike geometry has been inferred from the accompanying earthquake swarms; unless the dike breaches the surface leading to a fissure eruption, there is no direct knowledge of its location. The 1977 Krafla, Iceland, intrusion is particularly interesting in this regard because the advancing earthquake swarm [*Brandsdottir and Einarsson*, 1979] arrived at a geothermal field nearly coincident with the dike intersecting a geothermal borehole erupting a small volume of basalt tephra [*Larsen and Grönvold*, 1979], convincingly demonstrating that the seismicity marked the leading edge of the dike (Figure 3c). In some cases shallow normal faulting, which often forms grabens over shallow dikes, must have preceded the arrival of the dike tip [*Rubin*, 1992]. Indeed, during the 1977 Krafla intrusion, a highway was disrupted by surface faulting 1 h prior to the borehole eruption [*Rubin*, 1992].

[9] Geodetic observations, including GPS, tilt, and InSAR are commonly used to constrain the overall geometry of dike intrusions. However, geodetic observations have limited spatial resolution at depth. Seismicity responds to stress change, which scales with the spatial gradient of dike opening, and is thus sensitive to shorter wavelength features of the dike opening distribution. For this reason, including additional information from the spatiotemporal distribution of dike-induced earthquakes should improve spatial resolution at depth.

[10] The underlying assumption in this work is that dike opening both deforms the Earth surface and alters the stress field adjacent to the dike, potentially leading to earthquakes in the surrounding crust. We further assume that on the time scales of intrusions the stress changes are dominated by the elastic response of the surrounding crust and ignore thermal stressing as well as mechanically and/or thermally induced pore-pressure changes (see section 5). The response of seismicity to changes in stress acting on faults in the surrounding crust can be modeled using the seismicity-rate theory of *Dieterich* [1994], which is based on rate and state-dependent earthquake nucleation. The *Dieterich* [1994] theory is consistent with, and provides a physical

basis for, the Omori decay of aftershocks and has already been used to model seismicity-rate changes associated with dike intrusions [*Dieterich et al.*, 2000, 2003, *Toda et al.*, 2002] as well as slow slip events [*Segall et al.*, 2006; *Llenos and McGuire*, 2011].

[11] *Dieterich et al.* [2000, 2003] used the theory of *Dieterich* [1994] to invert observed seismicity-rate changes on Kilauea's south flank for stress changes within the volcano. They compared the inferred stress changes to those computed independently from elastic models of surface deformation. While not a formal joint inversion of seismic and geodetic data as presented here, these papers showed the power of analyzing both data types in a mechanically consistent framework. In particular, *Dieterich et al.* [2003] showed that south flank seismicity in the 3 month period following the 1983 ERZ dike injection requires a combination of deep rift opening and slip on the south flank decollement. We compare these conclusions to our results in section 5.

[12] *Segall and Yun* [2005] demonstrated that a joint inversion of synthetic seismicity and InSAR data significantly improved the spatial resolution of a dike at depth, relative to inversion of InSAR data alone. In this paper, we expand on that time-independent approach and develop a method for time-dependent dike propagation [*Llenos et al.*, 2010, 2011]. We use the *Dieterich* [1994] equations to relate stress changes caused by dike opening to seismicity-rate changes and combine these with elastic Green's functions to invert surface displacements and seismicity for dike length and pressure over time using a nonlinear least squares algorithm.

[13] The forward model specifies the spatially uniform excess pressure acting on the dike walls [*Yun et al.*, 2006]. This provides several advantages over kinematic approaches, which employ spatial smoothing constraints to regularize the inversion. Most importantly, the pressure boundary condition is motivated by the physics of the diking process. Secondly, these boundary conditions require fewer degrees of freedom in the inversion, compared to kinematic models in which the amount of opening on each patch of a dike must be solved for at each time step, thus obviating the need for regularization. Finally, the estimated pressure history can provide direct insight into the physical process driving the intrusion.

[14] We first review the method for forward simulation of deformation and seismicity and then introduce the inversion algorithm. After testing the method with simulated data we apply it to the 2007 Father's Day intrusion (Figure 1). The seismicity that occurred during the swarm is relocated and analyzed together with GPS and tiltmeter data [*Montgomery-Brown et al.*, 2011]. Our results suggest that the rapid down-rift expansion of seismicity reflects an apparent velocity involving a significant vertical component of dike propagation. The results are also sensitive to the vertical extent of dike opening relative to the earthquake depths and have implications for the background stressing rate within Kilauea's ERZ and along-strike variations in stressing and seismicity rates.

2. Method

[15] We model a dike intrusion as a rectangular crack, subjected to spatially uniform internal pressure, that propagates in an elastic half-space. We expect lateral propagation to dominate for shallow intrusions and to be the easiest to resolve, although future work should generalize the approach to consider vertical propagation. We thus assume in this work that dike height, depth, strike, and dip remain constant, while the dike length and magma pressure change with time. We combine a forward model for seismicity rate based on integration of the *Dieterich* [1994] equations with elastic Green's functions to invert surface displacements and seismicity for changes in dike length L and excess magma pressure Δp (magma pressure in excess of dike-normal stress) over time. We also solve for the time-independent constitutive parameter a and the background stressing rate $\dot{s}_r$ (both defined below).

2.1. Forward Modeling

[16] We assume a uniform pressure boundary condition on the dike walls. This cannot be the case at the dike tip [*Rubin and Gillard*, 1998; *Rubin et al.*, 1998]; however, the spatial scale over which the dike-tip variations occur may be sufficiently small that it influences the stress only in a small volume around the dike tips. Future studies should include the influence of the dike-tip zone, as well as depth dependence of excess pressure (see section 5). At each time step, the dike plane is subdivided into N_{el} grid elements, and the Boundary Element Method (BEM, specifically the Displacement Discontinuity Method) is used to obtain the dike opening $\delta(\xi)$ appropriate for the specified dike pressure, where ξ is spatial coordinate on the dike plane. The induced normal stress on the dike elements is a linear function of the dike opening; therefore, given the excess pressure boundary condition Δp and the elastic response functions A relating opening to normal traction in an isotropic, homogeneous, linear-elastic half-space, the opening distribution can be computed via

$$\delta(\xi) = A^{-1}\Delta p, \tag{1}$$

where Δp is a constant vector of length N_{el}. The surface deformation d is computed from elastic Green's functions G relating the dike opening to deformation [*Okada*, 1992, e.g.,]:

$$d(x, t_k) = G[L(t_k), x; \xi]\delta(\xi, t_k) = G[L(t_k), x; \xi]A^{-1}\Delta p(t_k). \tag{2}$$

The Green's functions depend on the dike length L, strike, depth, and so on, although in this implementation only length changes with time. To predict seismicity triggered by stress changes induced by the dike, we utilize the seismicity-rate theory of *Dieterich* [1994]. The theory is based on the time to instability of a population of independent sources that slip according to a rate- and state-dependent friction law and the assumption of constant seismicity rate under constant background stressing rate $\dot{s}_r$. Specifically, the model relates the seismicity rate R to stress changes via

$$R = \frac{dN}{dt} = \frac{r}{\gamma \dot{s}_r} \tag{3}$$

$$\frac{d\gamma}{dt} = \frac{1}{a\sigma}\left(1 - \gamma\frac{ds}{dt}\right), \tag{4}$$

where N is the number of earthquakes, r is the background seismicity rate, γ is a state variable, a is a frictional constitutive parameter (related to the "direct effect" in rate
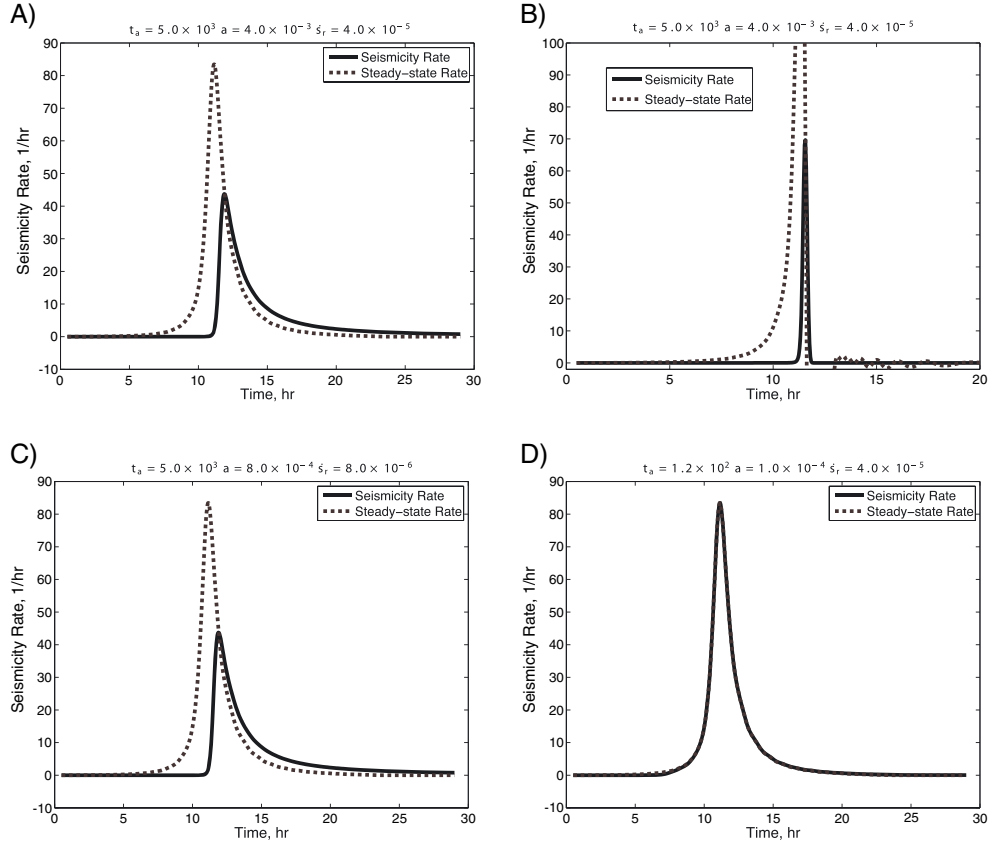
Figure 4. Predicted seismicity rate. (a) Voxel beneath dike; (b) voxel adjacent to dike; (c) scaling the parameters a and $\dot{s}_r$ in Figure 4a by a factor of 0.2, such that t_a remains the same; and (d) as in Figure 4a but decreasing a and hence t_a by a factor of 4. Stressing rate is proportional to steady state seismicity rate. In Figure 4b the stressing rate becomes strongly negative after the dike tip passes; slight oscillations are due to discreteness of the BEM representation.

and state-dependent constitutive laws), and s is a modified Coulomb stress defined by

$$s = \tau - \left(\frac{\tau}{\sigma} - \alpha \right) \sigma = \tau - (\mu - \alpha)\sigma, \qquad (5)$$

where τ is the shear stress, σ is the effective normal stress (normal stress in excess of pore pressure) acting on seismogenic faults, μ is the coefficient of fault friction, and α is a constitutive parameter relating changes in frictional state to changes in normal stress [*Dieterich*, 1994; *Linker and Dieterich*, 1992; *Dieterich et al.*, 2000]. For simplicity, and because the normal stress coupling is not well resolved by laboratory data, we set $\alpha = 0$ here.

[17] The parameter γ is inversely proportional to normalized seismicity rate, and thus can be interpreted as the time between earthquakes. Equation (4) has steady state solution $\gamma_{ss} = 1/\dot{s}$. We assume that initially $\dot{s} = \dot{s}_r$ ($\gamma_0 = 1/\dot{s}_r$) with seismicity steady state at background rate r. If $\dot{s} > (<) 1/\gamma$, then the time between events decreases (increases). Defining a nondimensional state variable $\gamma^* \equiv \gamma \dot{s}_r$, such that $R/r = 1/\gamma^*$, equation (4) can be written as

$$\frac{d\gamma^*}{dt} = \frac{1}{t_a} \left(1 - \gamma^* \frac{\dot{s}}{\dot{s}_r} \right), \qquad (6)$$

where $t_a \equiv a\sigma/\dot{s}_r$. Equation (6) makes clear that scaling the stressing rate $\dot{s}$, background stressing rates $\dot{s}_r$, and $a\sigma$ by a

constant (such that t_a is unchanged) leaves the seismicity rate unchanged (see Figures 4a and 4c).

[18] Given a piecewise linear stressing history (piecewise constant stress rate), equation (4) can be integrated to obtain an expression relating the state variable at time step k, γ_k, to the Coulomb stressing rate $\dot{s}_k$ at that time step:

$$\gamma_k = \left(\gamma_{k-1} - \frac{1}{\dot{s}_k} \right) \exp\left[\frac{-\dot{s}_k(t_k - t_{k-1})}{a\sigma} \right] + \frac{1}{\dot{s}_k}, \qquad (7)$$

where $\dot{s}_k = (s_k - s_{k-1})/(t_k - t_{k-1})$ and s is the stress change induced by the dike [*Dieterich*, 1994; *Segall et al.*, 2006]. The stress of course depends on the location of the fault relative to the dike, as well as the dike size, shape, and pressure. Combining (7) with (3) gives the seismicity rate

$$\frac{R_k}{r} = \left\{ \left(\dot{s}_r \gamma_{k-1} - \frac{\dot{s}_r}{\dot{s}_k} \right) \exp\left[\frac{-\dot{s}_k(t_k - t_{k-1})}{a\sigma} \right] + \frac{\dot{s}_r}{\dot{s}_k} \right\}^{-1}. \qquad (8)$$
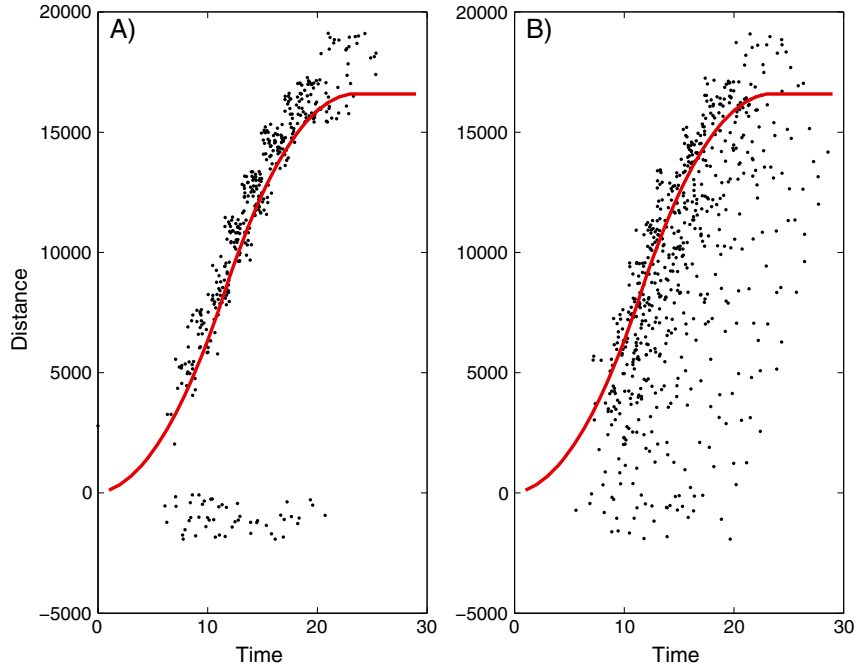
Starting from the background stressing rate, $\gamma_0 = 1/\dot{s}_r$.

[19] Integrating (8) yields N, the cumulative number of events triggered during the intrusion:

$$N(x,t) = r \frac{a\sigma}{\dot{s}_r} \sum_{k:t_k < t} f(\dot{s}_k(x)\,(t - t_{k-1}), \gamma_{k-1}\dot{s}_k(x)), \qquad (9)$$

where f is

$$f(u,v) = \ln\left[1 + \frac{\exp(u/a\sigma) - 1}{v} \right]. \qquad (10)$$

5

Figure 5. Predicted space-time distribution of seismicity (a) adjacent to dike and (b) below the dike. Earthquakes above the dike's top edge would appear comparable to those in Figure 5b. Black dots represent earthquakes randomly distributed within voxels in space and time based on predicted seismicity rate. Red curve represents position of leading dike tip.

[20] To generate forward models of seismicity associated with a propagating dike, the volume immediately surrounding the dike is divided into a number of volume elements (voxels). Very different behavior is predicted for voxels either above or below the dike (assuming seismogenic behavior occurring in both regions) from voxels adjacent to the dike. A voxel above or below the dike (Figure 4a) experiences a rapidly increasing stress rate as the dike tip approaches, followed by a decaying stress rate. This leads to a rapid increase in the seismicity rate followed by a decaying sequence of events. On the other hand, a voxel adjacent to the dike falls into a stress shadow (stress rate becomes strongly negative) after the dike tip passes. This results in a dramatic decrease in seismicity rate following the passage of the dike tip (Figure 4b).

[21] The differences in behavior lead to rather different predicted space-time patterns of seismicity, as illustrated in Figure 5. "Shallow seismicity" (that is shallower than the dike bottom but deeper than the dike top) initiates near the leading edge of the dike but shuts off rapidly as the dike tip passes. The distal ends experience a greater number of events because these volumes experience a positive stressing rate for a greater length of time. This seems to be the pattern observed in some of the Afar intrusions (Figure 3a and 3b). In contrast, seismicity below (or above) the dike is predicted to continue at a decaying rate, depending on t_a, after the dike tip passes. This pattern more closely matches that observed at Krafla (Figure 3c) and other swarm sequences.

[22] Notice from (8) that if $\dot{s}_k \Delta t_k / a\sigma = (\dot{s}_k/\dot{s}_r)(\Delta t_k/t_a) \gg 1$, the seismicity rate is steady state and proportional to the normalized stressing rate, $R_k/r = \dot{s}_k/\dot{s}_r$ (Figure 4d). Alternatively, if $\dot{s}_k \Delta t_k / a\sigma$ is positive but not large, time-dependent nucleation causes the seismicity rate to lag behind

the stressing rate. For a given dike pressure/length history (that is stress history), small values of $a\sigma$ favor steady state response, whereas larger $a\sigma$ promote an extended seismicity sequence analogous to an aftershock sequence. Indeed, we show in Appendix A that equation (8) reduces to Omori's law in the limit of a short duration event with high stressing rate, followed by a return to the background stressing rate.

[23] At each time step, elastic Green's functions are computed for a given dike length and pressure to obtain the displacement and tilt at observation points, as well as the stress change at observation points within each voxel. We have found that averaging over three points distributed along strike within each voxel yields a reasonably smooth seismicity rate; only evaluating stress at the voxel centers leads to a periodic fluctuation in seismicity resulting from the changing distance between the dike tip and the voxel centers. We assume that the reference seismicity rate r can be determined from the earthquake catalog prior to the intrusion. We also assume that effective normal stress σ is known; however, since σ only appears as the product $a\sigma$, estimates of a may reflect departures in effective normal stress from assumed values. For specified values of a and reference stressing rate $\dot{s}_r$, the stress change history is used in equations (8) and (9) to calculate the seismicity rate and cumulative number of events in each voxel at each time step. Some implementation details in the forward model calculations are discussed in Appendix B.

2.2. Nonlinear Inversion

[24] We combine the forward function for seismicity with elastic Green's functions to invert surface displacements and seismicity for changes in dike length and excess magma pressure as a function of time. Displacements are observed
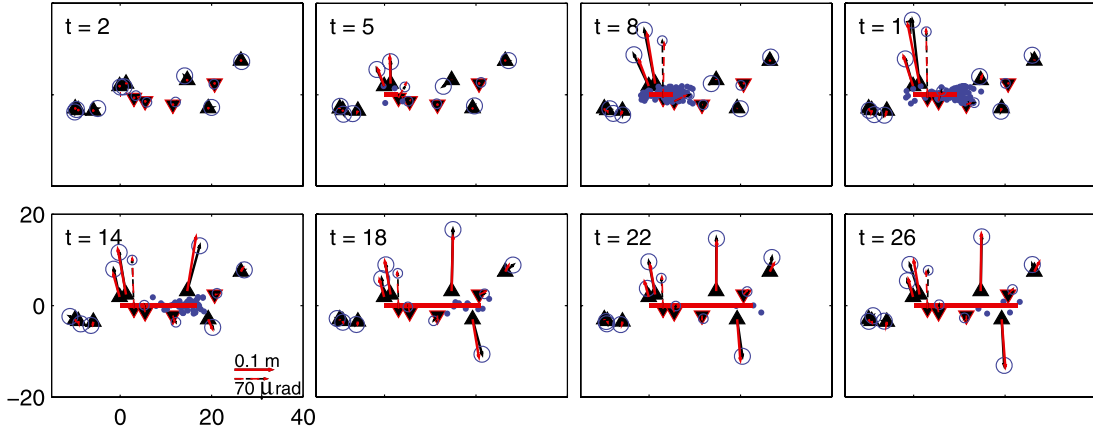
Figure 6. Observed (black) and predicted (red) displacements and tilts for simulation. GPS stations are upward triangles with solid vectors; tilt stations downward pointing triangles with dashed vectors. Simulated earthquake epicenters are shown as blue dots, and the estimated dike position is a horizontal red line. Map scale is in kilometers; time (hours) after onset of the intrusion indicated in each panel.

at N_{GPS} GPS stations, tilt at N_{tilt} tiltmeters, and seismicity in N_{obs} voxels observed at each of nt time steps. Therefore, the data vector consists of $3N_{\text{GPS}} \times nt$ GPS observations, $2N_{\text{tilt}} \times nt$ tilt observations, and $N_{\text{obs}} \times nt$ seismicity observations. The model $\mathbf{m}$ consists of the change in the dike length ΔL_k during the kth time step and excess pressure Δp_k at each time step, plus the time-independent parameters a and $\dot{s}_r$:

$$\mathbf{m} = [\Delta L_1, \Delta L_2, \ldots, \Delta L_{nt}, \Delta p_1, \Delta p_2, \ldots, \Delta p_{nt}, \dot{s}_r, a].$$

The dike length at epoch k is thus $L_k = \sum_{j=1}^{k} \Delta L_j$. ΔL_j are constrained to be nonnegative so that the dike length is a nondecreasing function of time.

[25] Because seismicity is a nonlinear function of the dike-induced stress change, we utilize a nonlinear least squares algorithm that minimizes the weighted L2 norm of the misfit between the observed and predicted data over all nt epochs:

$$\Phi = \sum_{k=1}^{nt} \left\{ \left\| \Sigma^{-1/2}(\mathbf{d}_k - \hat{\mathbf{d}}_k) \right\|^2 + \kappa^2 \left\| N_k - \hat{N}_k \right\|^2 \right\} \qquad (11)$$
$$+ \kappa_2^2 \sum_{k=1}^{nt-1} (\Delta p_{k+1} - \Delta p_k)^2,$$

where $\mathbf{d}_k$ and $\hat{\mathbf{d}}_k$ are the observed and predicted deformation data, Σ the data covariance matrix, N_k and $\hat{N}_k$ the observed and predicted number of earthquakes in each voxel, and κ^2 is a scaling factor that weights the seismicity residuals relative to the deformation residuals. We choose the scaling factor such that the maximum of the absolute value of the seismicity and deformation residuals are comparable. The last term in the objective is added to penalize temporally variable dike pressure histories; without this regularizing term the estimated dike pressure tends to be unreasonably variable in time.

[26] We employ the cumulative number of events N (in each voxel), rather than seismicity rate R, in the objective function because, especially with small numbers of events, cumulative earthquake count is more stable. In addition, as seen in Figure 4, the seismicity rate can be quite localized in time such that the residuals are near zero most of the time. We have observed that the optimization is more

prone to local minima when there are no seismically active voxels above or below the dike. As discussed previously, voxels adjacent to the dike pass into a stress shadow causing the seismicity rate to drop dramatically. The cumulative number of events in a voxel is thus fixed once a dike tip passes. The optimizer tends to fit the cumulative number of events in each voxel but then has a difficult time fitting the passage time of the dike tip. To overcome this, we have added a term to the objective (11) that penalizes the time difference between the observed and predicted times of maximum seismicity rate. Specifically, this term is the sum over voxels of the square of the time difference between the peak of observed and the peak of predicted seismicity rate, $\kappa_3^2 \sum^{Nvox}(t_p - \hat{t}_p)^2$. The time of peak observed rate in a voxel t_p is the earliest time having the maximum rate for that voxel. To keep the objective continuous (except when a peak is in the first or last time bin), differentiable, and locally informative (nonzero gradient away from a minimizer), the time of peak predicted seismicity $\hat{t}_p$ is obtained as the maximum of a parabolic fit to the three time points supporting the maximum predicted rate. Each separate term is weighted proportional to the peak number of observed events. This improves the ability of the optimization to track the timing of the down-rift extent of seismicity. The trade-off is that it adds an additional weighting parameter κ_3 to the objective (11).

[27] The objective function is minimized subject to the bound constraints using the MATLAB nonlinear least squares solver `lsqnonlin` that employs a trust-region reflective algorithm [*Coleman and Li*, 1996]. Some implementation details are discussed in Appendix B.

3. Simulations

[28] To test the inversion algorithm, we simulate noisy seismicity and surface deformation observations for a dike that propagates unilaterally to the east at variable rate, ultimately reaching a length of 23 km over a 29 h time period (Figure 6). The dike is vertical and extends from 500 m beneath the surface to a depth of 5 km. The dike-length and excess pressure history are illustrated in Figure 7. The
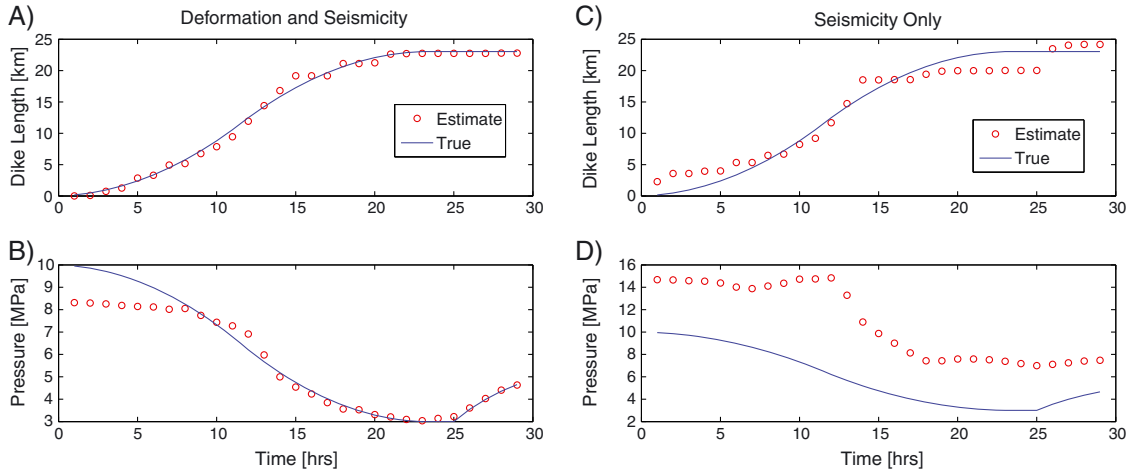
Figure 7. Comparison of input and estimated history of (top) dike length (km) and (bottom) excess dike pressure (MPa) for simulation. Simulations with (left) both geodetic and seismic data and (right) only seismicity data.

input dike pressure decreases as the magma chamber feeding the eruption drains and then slightly recovers after dike propagation ceases (Figure 7).

[29] The simulated deformation data come from eight GPS receivers and four tiltmeters; locations are illustrated in Figure 6. Normally distributed random noise was added to the synthetic data with a magnitude of 20% of the mean of the final GPS displacements and tilts. Seismic data were synthesized in 98 voxels surrounding the dike. The reference seismicity rate r is taken to be 0.002 events/h (one event every $\sim$ 21 days); the reference stressing rate is $\dot{s}_r = 4 \times 10^{-5}$ MPa/h (0.35 MPa/yr). The effective normal stress σ is uniformly 50 MPa, and the friction parameter a is 0.004. The characteristic time t_a is thus 5000 h or $\sim$ 210 days. The simulated seismicity was computed on vertical strike-slip faults oriented 30° counterclockwise from the dike plane, while in the inversion it was assumed (incorrectly) that the faults were oriented 30° clockwise from the dike plane. Likewise, the coefficient of friction used to generate the data was 0.6, while in the inversion we assume 0.4. Noise in seismicity data comes from imprecise earthquake locations. Random event locations were computed from the predicted seismicity rate assuming a uniform spatial distribution within each voxel. Random location errors were then assigned to each event with a standard deviation of 0.75 km (comparable to the voxel dimensions) and the event count per voxel computed based on the perturbed locations.

[30] For the inversion the initial estimate was intentionally set to be far from the true input model. The initial dike-length increments ΔL_k were 5% of the average increment (total length divided by number of epochs), the dike pressure was initially set to 5% of the mean pressure, and $\dot{s}_r$ and a were perturbed by factors of 5. The lower and upper bounds on dike-length increment were set to 1 m and 25% of the final length, respectively. The dike pressure is bounded between zero and 3 times the maximum pressure, while the bounds on $\dot{s}_r$ and a were factors of 10 above and below the true value. Reasonable results are obtained with weights on the seismic residuals 20% of the weight on the deformation residuals ($\kappa = 0.2$ in equation (11)). For $\kappa \gg 0.2$ the deformation data are essentially ignored. The constant for

smoothing the pressure differences was set to $\kappa_2 = 10$ based on visual inspection.
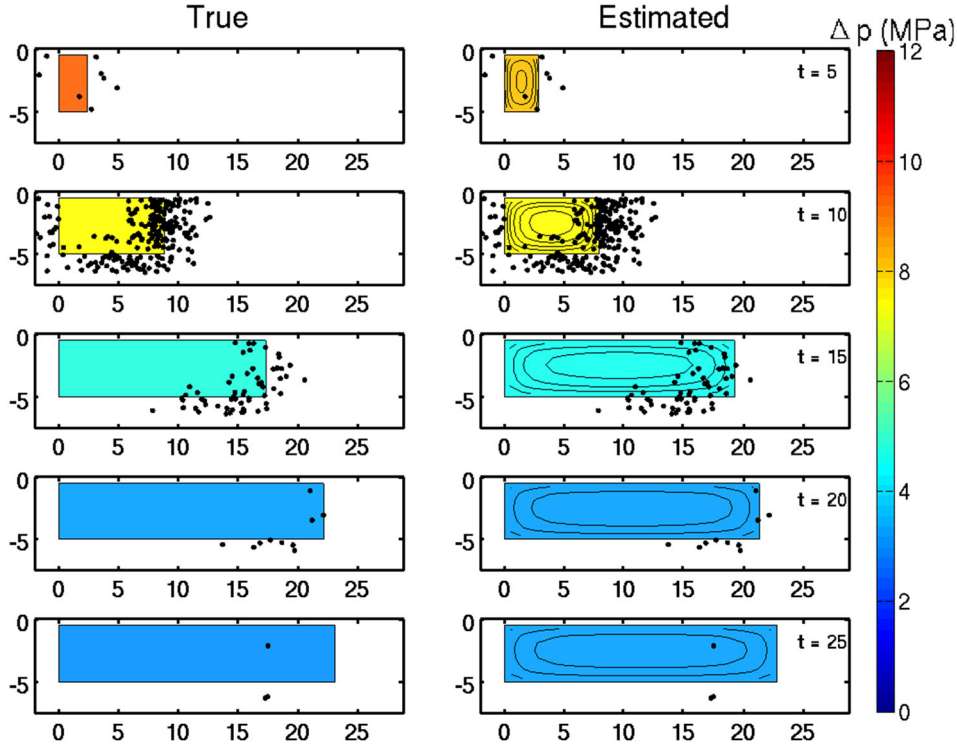
3.1. Simulation Results

[31] The estimated dike-length and pressure history are shown in Figure 7 (left). The dike-length history is recovered remarkably well. The excess dike pressure is underestimated (by about 20%) at early time but is reasonably well estimated for $t \geq$ 7 h. At early times the dike is short and generates relatively little measurable deformation, and the pressure during this period is thus poorly constrained. The inferred dike model does a good job of reproducing both the spatial and temporal pattern of displacements and tilts (Figure 6). A comparison between the input and estimated dike length, pressure, and seismicity is shown in Figure 8. The estimated background stressing rate $\dot{s}_r$ is a factor of 1.5 greater than the true value, while the friction parameter a is 68% of the input value. The ratio $t_a = a\sigma/\dot{s}_r$ is thus biased low by a factor of 2.3.

[32] The conclusion of this test is that the algorithm can recover the dike-length and pressure history reasonably accurately even in the presence of significant noise, and with some incorrect modeling assumptions about the fault plane orientations and coefficient of friction. Of course this does not prove that additional assumptions, particularly the validity of the seismicity-rate model, are valid in the Earth.

[33] Before testing the method on actual data we perform one additional test removing deformation data from the objective function, so that the estimation is controlled completely by seismicity. Results are shown in Figure 7 (right). The algorithm does a good job of recovering the dike length simply from the migration of the earthquake swarm. Without deformation data, the recovered excess magma pressure is inaccurate, as expected. The limited constraint on pressure arises because the stressing rate is a function of pressure. However, with a weaker constraint on pressure we expect that the seismicity-rate parameters will be less well constrained. This is indeed true; $\dot{s}_r$ is a factor of 3.5 greater than true, while a is a factor of 1.3 larger. The average dike pressure is also a factor of 2.0 (range 1.5 to 2.5) greater than the input, such that t_a is biased low by a factor of 2.7.

Figure 8. Simulation results: comparison between (left) input dike model and (right) that estimated from inversion. Plan view looking horizontally at dike. Color maps excess dike pressure; contours in right column are curves of constant dike opening. Earthquake hypocenters randomly located within voxels for both input and estimated models.

Equation (6) showed that the seismicity-rate equations are invariant to scaling by a constant factor. Increasing the dike pressure by a factor of somewhat greater than 2 increases the stress rate by a comparable amount. (Let $s = \Delta p f(L)$, such that $\dot{s} = \Delta \dot{p} f(L) + \Delta p (\partial f/\partial L)\dot{L}$, where the second term tends to dominate the stress rate.) Scaling the background stressing rate and $a\sigma$ by the same amount leaves the predicted seismicity unchanged. This example shows that even weak geodetic constraints help to determine the seismicity-rate parameters. Of course, well-located geodetic measurements also help constrain the overall dike geometry.
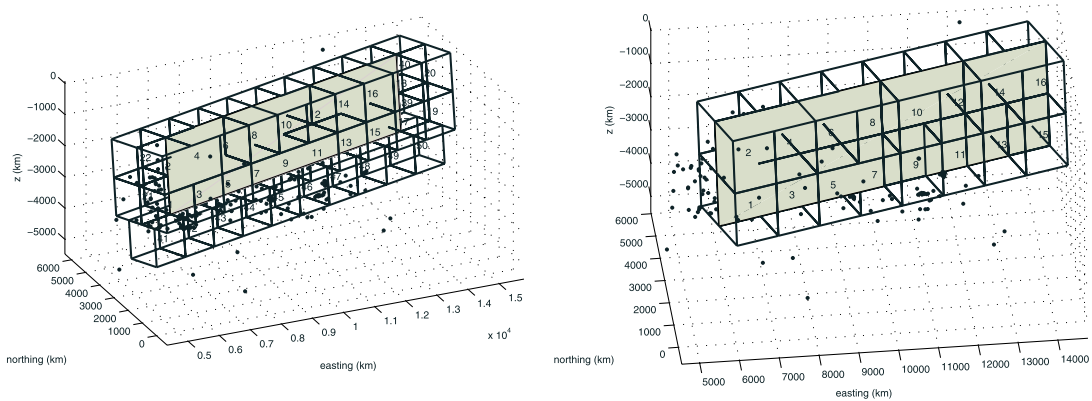
4. The 2007 Father's Day Intrusion, Kilauea, Hawaii

[34] We apply the joint inversion method to the "Father's Day" intrusion [*Poland et al.*, 2008] that occurred over roughly 2 days beginning on 17 June 2007 in the East Rift Zone (ERZ) of Kilauea (Figure 1). The intrusion began with the onset of increased seismicity and tilt at stations UWE (at Kilauea summit) and ESC (in the ERZ) at decimal day 17.51 [*Poland et al.*, 2008]. *Montgomery-Brown et al.* [2010] found that the cumulative GPS, tilt, and InSAR changes over the course of the intrusion are best explained by a pair of en echelon dikes that strike 67°, following zones of ground cracking parallel to the ERZ, and dip 80° to the south. The dikes extend from near the surface to a depth of ~2.5 km. Analysis of kinematic GPS and tilt data reveal that the intrusion occurred in two stages corresponding spatially and temporally with rift zone seismicity

[*Montgomery-Brown et al.*, 2011]. The dike initiated on the western of the two segments before jumping to the eastern segment, where the largest dike opening occurred. The dike breached the surface only at its distal, eastern end at Kāne Nui O Hamo, where a small volume (1500 m^3) of basalt erupted.

[35] The Hawaii Volcano Observatory recorded roughly 250 earthquakes of $M \geq 1.5$ during the intrusion. The earthquakes were relocated following the approach of *Syracuse et al.* [2010]. We combined rift and decollement seismicity recorded by the permanent HVO network and a variety of temporary seismic networks, including the SEQ network, which consisted of 20 broadband instruments on the south flank of Kilauea from February to August 2007. Data for a total of 3100 earthquakes, including ~400 associated with the Father's Day intrusion, were jointly inverted for hypocentral locations and three-dimensional V_p and V_s structure, with 2 km grid spacing in each direction in the central part of the model. Locations and velocities were calculated using the double-difference tomography algorithm `tomoDD` [*Zhang and Thurber*, 2003], which employs absolute arrival times to establish the coarser features of the velocity model and seismicity distributions and includes catalog and cross-correlated differential times to refine their smaller-scale features. To further improve locations during the Father's Day intrusion, earthquakes from May through July 2007 were relocated in the final three-dimensional velocity model obtained from the tomographic inversion.

[36] We correct the earthquake depths for the mean elevation above sea level of the nearby GPS stations to put

Figure 9. Voxel model for 2007 Father's Day intrusion in Kilauea's East Rift Zone viewed from the southwest. Dots are relocated earthquake hypocenters. (left) Shallow dike model; (right) deep dike model.

both deformation data and earthquake locations relative to the same vertical datum. Secondly, we notice that earthquake locations are slightly biased north relative to the best fitting dislocation (discussed below). This could potentially be due to the 3-D velocity model used to locate the seismicity while the deformation Green's functions are for a homogeneous half-space. We thus shift the earthquake locations south by ~ 700 m, so that they are roughly evenly distributed on either side of the dike.

[37] We anticipate that application of the method to the Father's Day event will be challenging for a number of reasons. First of all, the dike is not very long compared to the instrument spacing. In addition, the earthquake locations have significant uncertainty relative to the depth of the dike. Both factors limit spatial resolution. Second, as described above, *Montgomery-Brown et al.* [2010] have shown that the deformation data are not well fit by a single dike. We chose not to add the complexity of multiple en echelon segments, retaining the simpler model at the expense of a somewhat degraded fit to the data. Third, our simplified model considers only lateral propagation, with the upper and lower edges of the dike at fixed depth. This does not account for the shallowing of the dike at its eastern terminus where it breached the surface; as discussed below this also degrades the data fit. Fourth, the simplification of lateral dike propagation at fixed height is nonphysical at the onset of the intrusion. In the limit this model posits a vanishingly short dike with the full depth extent of the final intrusion; at the onset the model dike is a vertical line. In reality the dike grows both vertically and laterally, particularly at the onset of the intrusion. For this reason we do not attempt to fit seismicity during the earliest phase of the intrusion. Specifically, we exclude data from voxels nearest the nucleation region (the western end) from the objective function for all time steps.

[38] It is instructive to contrast the current approach with standard kinematic inversions [e.g, *Montgomery-Brown et al.*, 2011], in which the spatial distribution of dike opening is adjusted to fit the data, without regard to a pressure boundary condition. In the present model the opening is governed by a spatially uniform excess pressure, together with the dike size and shape. There are thus far fewer degrees of freedom compared to kinematic inversions, which should be accounted for when comparing results from these two approaches.

4.1. Inversion Setup

[39] We focus on the first 2 days of the intrusion, which saw the greatest changes in seismicity and deformation rate. We also include data for 6 h prior to the onset of seismicity and tilt. Data are analyzed from the two closest tiltmeters (ESC and POO) and the five GPS stations nearest the intrusion (NUPM, KTPM, GOPM, PGF2, and HALR) (Figure 1). Although the GPS data were originally processed at 4 min intervals [*Montgomery-Brown et al.*, 2011], we model the GPS and tilt data at hourly epochs. Based on data prior to the intrusion, standard deviations in the GPS displacements are roughly 1–2 mm in the horizontal components and 2–3 mm in the vertical. Standard deviations in the tilt are $\sim 0.2\,\mu$rad at ESC and $\sim 0.03\,\mu$rad at POO. Given the overly simplified nature of the geometric model, we do not expect to be able to fit the data at this level.

[40] The volume adjacent to the dike is divided into 50 voxels, with two rows of 10 voxels on each side of the dike and one row immediately below the dike (Figure 9, left). Earthquakes that fall outside the voxels are mapped to the nearest voxel. The westernmost three columns of voxels, closest to the dike nucleation zone, are excluded from the objective function (including voxels 41–43). We estimate a reference seismicity rate r based on a 5 year catalog of East Rift Zone seismicity from the Hawaii Volcano Observatory, adjusted to match the magnitude completeness of the relocated catalog of events during the Father's Day intrusion. Given that the relocated earthquakes are strongly concentrated in the deepest voxels, we adjust the background rate to reflect a presumed concentration of background seismicity at depth. This leads to $r \simeq 0.02$ events/hour/voxel for the deepest voxels, uniform along strike. Given the near absence of events in the shallower voxels, we eventually eliminated them from the objective function. The sparsity of shallow events could be due either to a background stress concentration at depth due to deep rift opening, as discussed in the Introduction, or to a transition to velocity strengthening friction at shallow depth such that earthquakes do not nucleate in this region.

[41] Given that the regional tectonics requires that the least principal stress must be nearly horizontal and normal to the ERZ, we expect either strike-slip or normal events. Double-couple focal mechanisms were calculated using the HASH algorithm [*Hardebeck and Shearer*, 2002], which uses
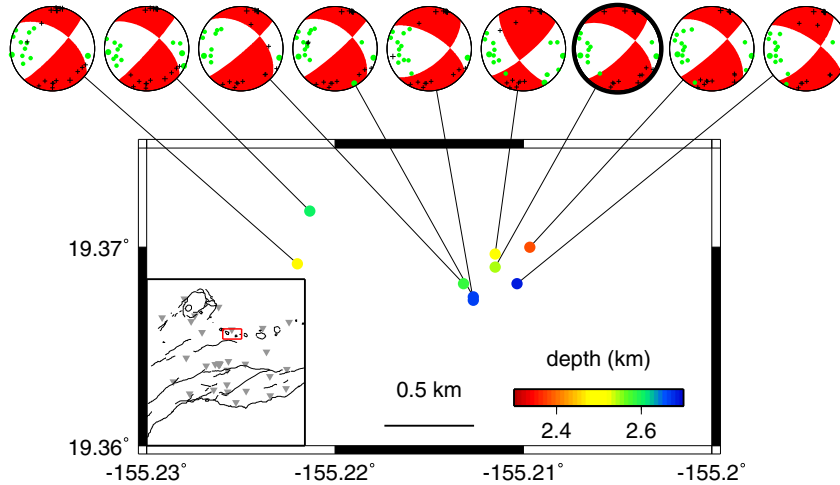
Figure 10. Focal mechanisms for better constrained earthquakes during the Father's Day intrusion. The outlined mechanism is for a $M\,2.2$ earthquake on 26 May 2007. The others occurred during the Father's Day event. Focal mechanisms are lower-hemisphere projections showing polarities (green circle = positive first motion, compressional; black cross = negative first motion, dilatational).

P wave first motions and model uncertainties to calculate the most likely solution for each earthquake. Takeoff angles and azimuths were calculated using the hypocenters and three-dimensional V_p model described previously. (Discussion of reversed polarities at several HVO stations appears in Appendix C.) The nine highest-quality focal mechanisms are shown in Figure 10. The outlined mechanism is for a $M\,2.2$ earthquake on 26 May 2007, while the remaining eight are for $M\,2.2$–2.6 earthquakes within a 5 h period on 17 June 2007. Consistent with expectations, the focal mechanisms predominantly show oblique right-lateral motion along near-vertical slip planes oriented at N46°E. The general similarity between the focal mechanism for the May and 17 June earthquakes indicates that the absolute stress state did not change substantially during the intrusion.

[42] We thus compute the stress changes on (near) vertical planes oriented at $\pm30°$ from the dike plane. The coefficient of friction is assumed to be 0.6 and the background normal stress and pore-pressure lithostatic and hydrostatic, respectively. This does not account for the extensional stress regime within Kilauea's ERZ. Thus, estimates of the friction parameter *a* will include a contribution from the deviation of the effective normal stress from the assumed background state (see section 5).

[43] We assume an overall dike geometry consistent with kinematic models of the intrusion [*Montgomery-Brown et al.*, 2010, 2011] but adjusted to account for the single dike segment with fixed top and bottom depth. This overly simplified geometric model is incapable of fitting both the tilt at ESC and the GPS displacement at NUPM (Figure 11). We find that a reasonable compromise is achieved with a dike that strikes N73°E, dips 85° south, with height (in the dip direction) of 2.4 km. Figure 11 illustrates the difficulty in fitting the cumulative deformation over the 2 days of the intrusion with the restricted geometric model, varying only the depth to the top of the dike. Recall that the
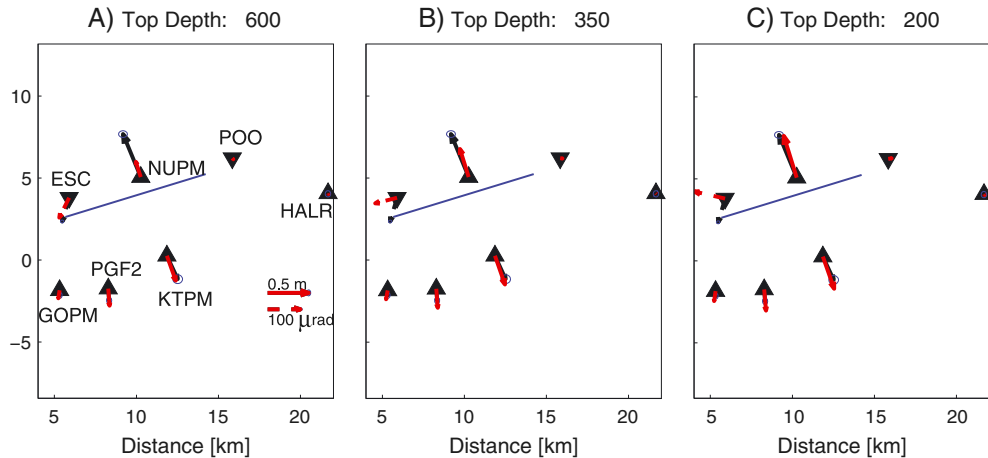
Figure 11. Influence of depth to the top of the dike on cumulative displacement and tilt (dashed). Observed (black with error ellipses inflated by a factor of 10) and predicted (red) vectors. Dike is subject to spatially uniform excess pressure of 8.5 MPa. Top of dike at (a) 600 m, (b) 350 m, and (c) 200 m.
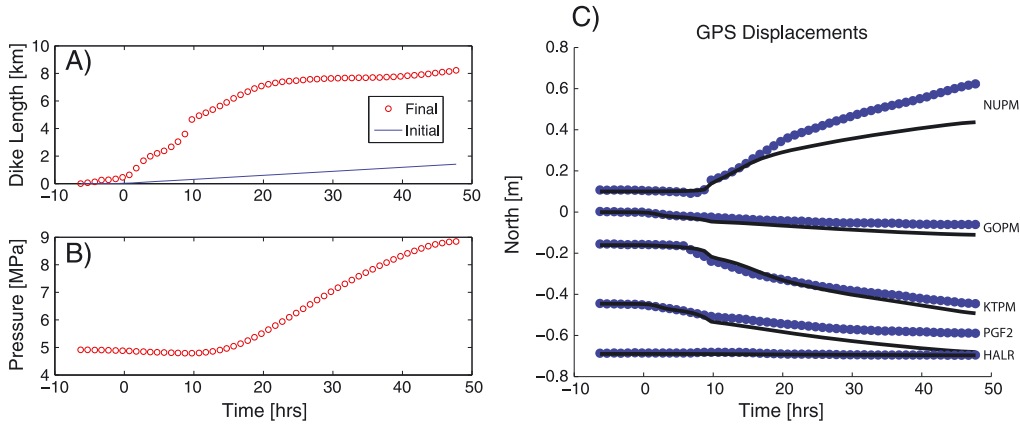
Figure 12. Inversion results with deformation data only. (a) Dike length as a function of time. "Initial" indicates starting model for the optimization. (b) Dike excess pressure as a function of time. (c) Fit to north component of GPS data. Blue circles, observed with 2σ error bars; black, predicted.

dike is buried at its western end but breached the surface near its eastern terminus. The direction and magnitude of the tilt at ESC is well fit when the top of the dike is at 600 m; however, the displacement at NUPM is underpredicted. If the top of the dike is only 200 m, the fit to the displacements at NUPM and the other GPS sites is reasonable; however, the fit to the tilt azimuth at ESC is poor. We take a top depth of 350 m as a reasonable compromise, given the limitations of the dike geometry model. Nevertheless, we down-weight the tilt data relative to GPS by a factor of 10, in part because of the possibility that tilt at ESC is influenced by ground cracking near the top of the dike (E. Montgomery-Brown, personal communication, 2012).

### 4.2. Results: Deformation Only

[44] As an initial step we invert the GPS and tilt data alone. The tilt is down-weighted relative to the GPS data by a factor of 10; the temporal smoothing parameter κ_2 was set to 200 based on subjective assessment of the dike pressure history in preliminary runs. Figure 12 shows the resulting dike-length and excess pressure history. The dike grew to an ultimate length of $\sim$ 8 km, mainly in the first 20 h of the

intrusion. Roughly 15 h after the onset of seismicity the dike pressure began to increase from $\sim$ 5 MPa to nearly 9 MPa. This is required to fit the gradually increasing GPS displacements during this time interval (Figure 12c), although allowing the depth extent of the dike to change would somewhat mitigate this increase in pressure. Because the top of the dike is restricted to a fixed depth, the final displacement at NUPM is underpredicted (as in Figure 11b). The displacement at PGF2 is slightly overpredicted.

[45] Figure 13 shows the dike length and seismicity, as well as predicted GPS displacements and tilts in map view. As noted above, the tilt has been significantly down-weighted and is consequently poorly fit. While the general fit to the GPS and seismicity data is reasonable, there is a clear tendency for the dike to lag behind the seismicity between 7 and 10 h after the onset of the intrusion. We address this with inversions that include seismicity in the objective function in the following sections.

4.3. Secondary Seismic Events

[46] Examination of the seismicity indicates an abundance of secondary events (aftershocks) in the swarm
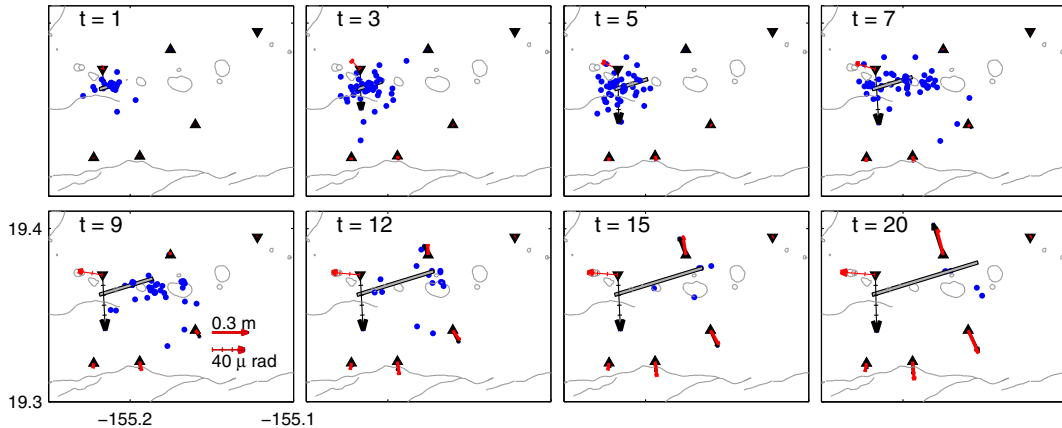
Figure 13. Map view of dike and predicted displacements and tilts (barbed vectors) for inversion with deformation only. Observed (black) and predicted (red) GPS displacements and tilts. Blue dots represent earthquake epicenters during the preceding 3 h.
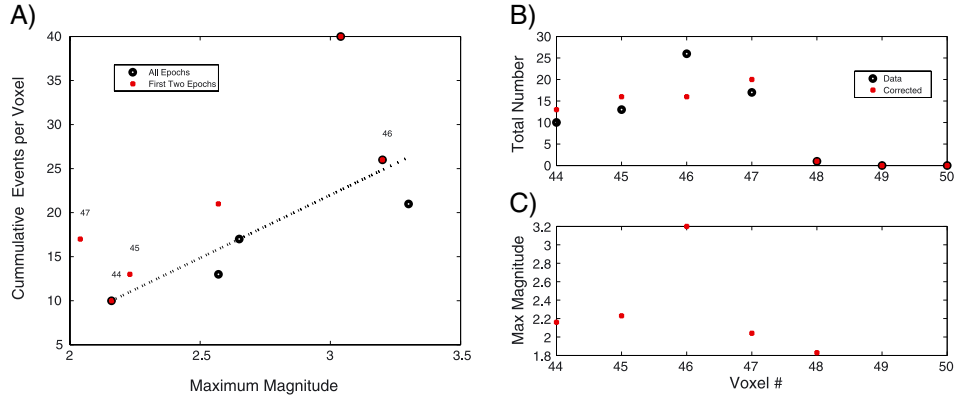
Figure 14. Secondary earthquakes. (a) Correlation between maximum magnitude M_{max} in each voxel and the cumulative number of events in that voxel. Red closed circle indicates M_{max} during the first 2 h for which seismicity occurs in that voxel, whereas blue open circle indicates M_{max} for all epochs. The straight line illustrates the L1 fit to M_{max}. (b) Cumulative number of events (sum over all epochs) versus voxel number for the deepest voxels. "Data" indicates original relocated catalog data; "Corrected" indicates renormalized values accounting for M_{max} correlation as described in text. (c) Maximum magnitude in each voxel.

earthquakes. This significantly complicates the analysis because the *Dieterich* [1994] equations, (3) and (4) in this paper, do not themselves account for the stress interaction between events and thus do not model secondary events. (This would require predicting, at least in some average sense, the location and magnitude of all earthquakes.) The evidence for secondary events is illustrated in Figure 14a, which shows the correlation between the maximum magnitude, M_{max}, in a voxel and the cumulative number of events in that voxel. Only the deepest voxels, which contain the preponderance of events, are shown. The straight line in Figure 14a indicates an L1 regression on M_{max}. The prominent outlier, the voxel with the most earthquakes (number 42), is located where the dike nucleated, a region that cannot be fit by the constant depth dike source, and is thus excluded from the objective function. We remove the dependence of N on M_{max}, preserving the relative time dependence of the seismicity in each voxel, as well as the total number of events

in voxels 44–50. This is shown as "corrected" in Figure 14b. Notice that the original data show a spike in seismicity in voxel 46, due to a relatively large ($M\,3+$) event. The fact that this particular voxel happened to experience a larger event, and therefore many secondary earthquakes, is outside the domain of the nucleation-only seismicity-rate theory. The corrected total number of events is a much smoother function of down-rift coordinate (voxel number) and therefore more amenable to inversion. Future work could consider a forward model that explicitly accounts for secondary events making use of observed earthquake magnitudes (see section 5).

4.4. Results: Deformation and Seismicity

[47] We first explore results with the dike geometry as illustrated in Figure 9, that is, with the majority of the earthquakes below the bottom edge of the dike. The estimated dike length and excess pressure from a combined inversion
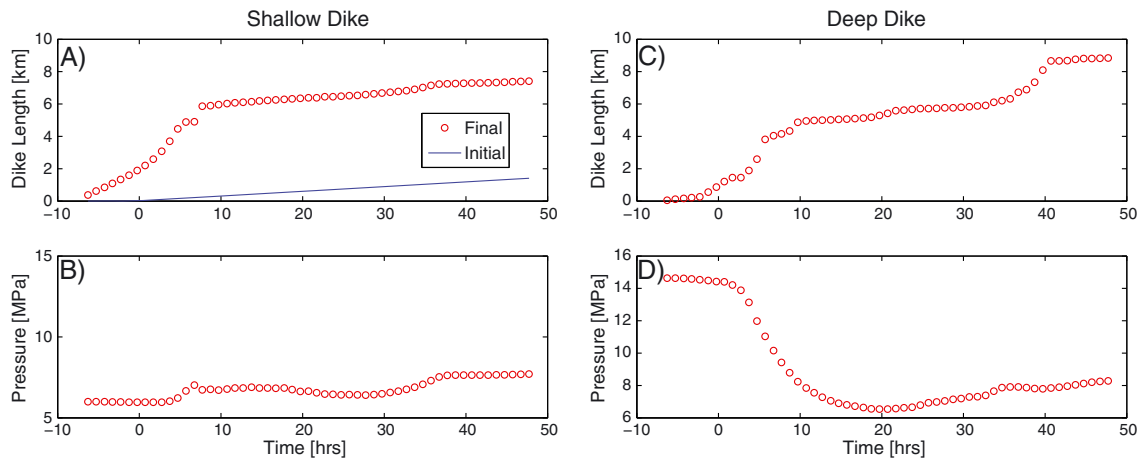
Figure 15. Father's Day inversion results including seismicity and deformation data. (a) Dike-length history for shallow dike; "Initial" indicates starting model for the optimization; (b) excess dike pressure. (c) Dike-length history for deep dike. (d) excess dike pressure.
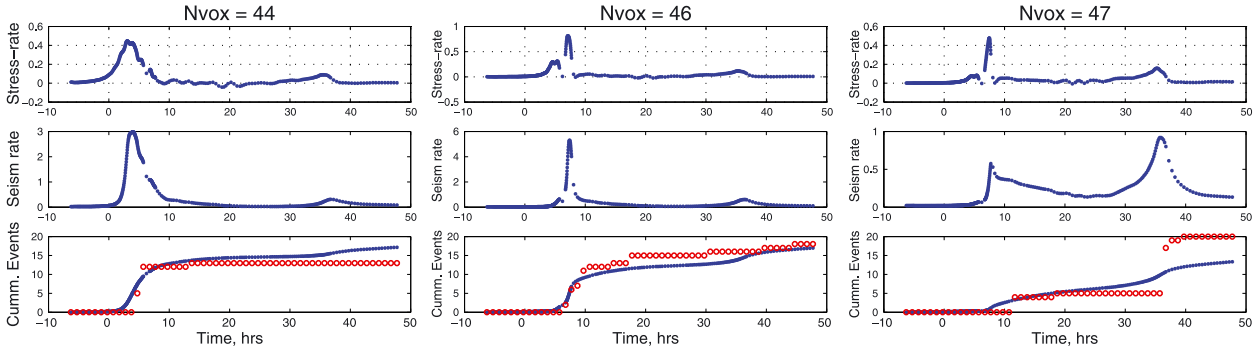
Figure 16. Seismicity history for selected voxels below the dike bottom during Father's Day intrusion. (top row) Stressing rate, (middle row) computed seismicity rate, and (bottom row) cumulative number of events. Open circles show observed number of events. Density of dots indicates the time stepping required by the algorithm to yield a sufficiently well-resolved stress rate.

of deformation and seismicity data ($\kappa = 50, \kappa_2 = 500$) are shown in Figure 15a. In this case the dike extends down-rift rapidly during the first 8 h of the intrusion and then grows more slowly. The excess pressure increases from about 6 MPa to almost 8 MPa.

[48] That the inferred dike model fits the seismicity data reasonably well is demonstrated in Figure 16, which compares the predicted and observed seismicity in three voxels near the bottom of the dike. The seismicity in voxel 44 increases dramatically after hour 5 and is matched reasonably well by the model prediction. Seismicity in voxel 46, which initiates only slightly later than in its westerly neighbor, is also quite well fit. Earthquakes in voxel 47, farther to the east, did not begin until hour 10 but then shows a large increase after hour 35. The data are reasonably well fit, although the model underpredicts the later jump in seismicity.

[49] The inversion converges to $a = 0.0025$. This is somewhat less than, but in the range of, laboratory values of a. For the assumed effective normal stress of slightly less than 50 MPa this corresponds to $a\sigma = 0.12$ MPa. This might indicate that σ is substantially less than assumed based on lithostatic stress and hydrostatic pore pressure (see section 5). The background stressing rate is estimated to be $\dot{s}_r \simeq 2.8 \times 10^{-3}$ MPa/h, corresponding to an unrealistically

high ~25 MPa/yr. Together, these values correspond to a characteristic time of $t_a \simeq 43$ h, which is very short, but required with this geometry to fit the rapid decay in seismicity rate following the passage of the dike tip. Different inversions that heavily weight the seismicity data yield similar results, namely, small t_a and very high background stressing rates.

[50] The good fit to the space-time evolution of swarm seismicity comes at the expense of degraded fit to the GPS data. The rapid eastward propagation in this model causes a jump in the predicted displacements at $t \simeq 5$ h that is not observed in the data. In summary, the best fitting models with the dike bottom shallower than the concentration of earthquakes are lacking on two accounts. First, it is not possible to fit the time evolution of the seismicity and GPS data with a single model. Weighting the GPS data heavily causes the dike tip to trail the seismicity during the rapid down-rift propagation phase (see Figure 17). On the other hand, weighting the seismicity heavily causes the model to predict substantial deformation earlier than observed in the GPS data. Secondly, the short decay time in the earthquake rate can only be achieved in this geometry with a very short t_a, which implies an unreasonable high stressing rate. These conclusions are robust to modest perturbations in the earthquake locations, to different starting models in
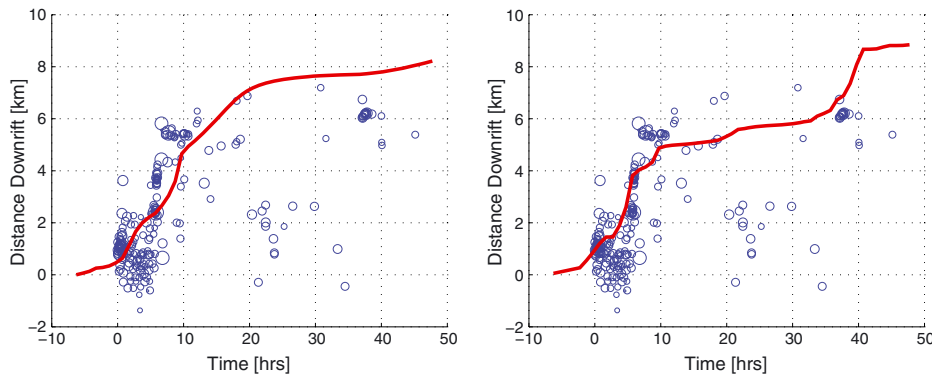
Figure 17. Space-time evolution of seismicity and inferred dike tip. Distance measured relative to the western dike tip in direction parallel to model dike. (left) Inversion based on deformation data alone ($\kappa = 0$). (right) Inversion with seismicity data ("Deep Dike" model). Size of circle reflects earthquake magnitude.
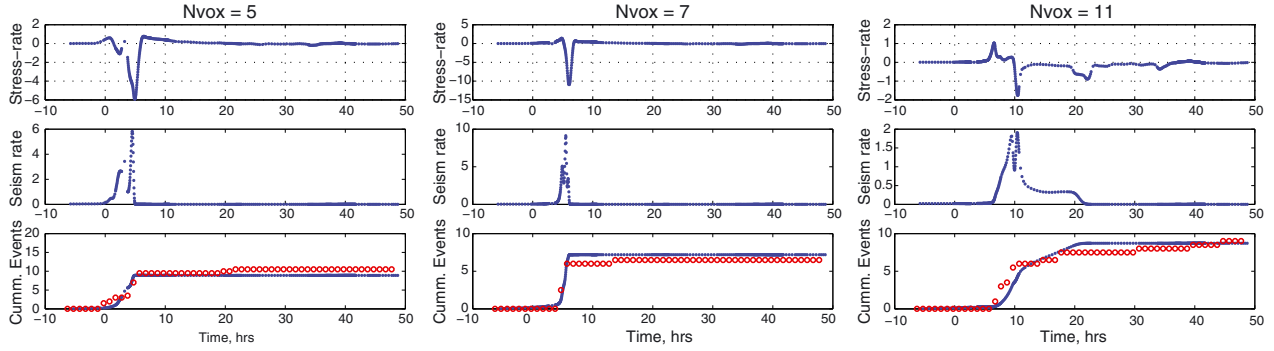
Figure 18. Seismicity history for selected voxels during Father's Day intrusion for the "Deep Dike" model in which the voxels are shallower than the dike bottom. (top row) Stressing rate, (middle row) computed seismicity rate, and (bottom row) cumulative number of events. Open circles show observed number of events. Density of dots indicates the time stepping required by the algorithm to yield a sufficiently well-resolved stress rate.

the inversion, and to changes in relative weighting in the objective function.
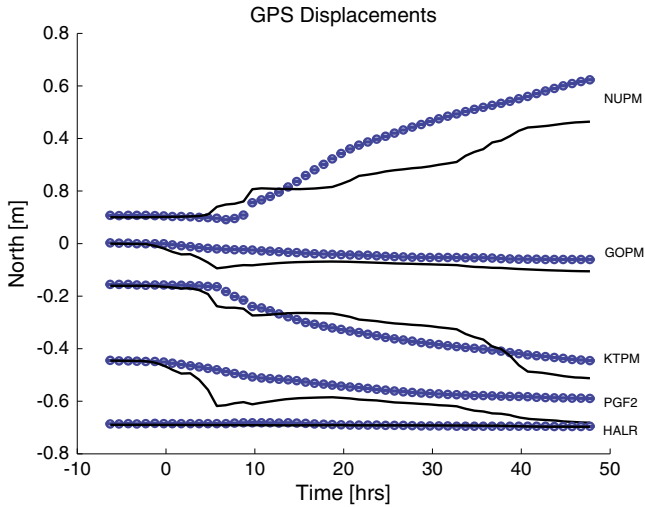
4.5. Deep Dike Results

[51] The deep dike geometry, in which the dike extends below the depth of seismicity, predicts very different space-time seismicity patterns (Figure 5). In particular since voxels adjacent to the dike fall into stress shadows, small t_a is not required to fit the rapid decay in seismicity with time. On the other hand, the voxels off the end of the dike are subjected to positive stressing for a longer period of time (Figure 2) and would thus be predicted to exhibit a large number of earthquakes if the background seismicity rate is uniform along strike. In contrast, the distal end of the swarm exhibited relatively few earthquakes, as seen in Figure 14 and in map view in Figures 13 and 19. Preliminary runs indicated that it was indeed not possible to satisfactorily fit the data with spatially uniform properties. A possible explanation for the paucity of events at the eastern terminus is that the 2007 dike ended in a region in which the stress was greatly relaxed by the 1997 Napau intrusion [*Owen et al.*, 2000a]. For the sake of exploration, we introduced a linear along-strike decrease in background seismicity rate r, such that average value was unchanged but r drops to zero in the easternmost voxel.

[52] We previously noted that the accuracy of the earthquake locations relative to the geodetically resolved dike is insufficient to determine which side of the dike the events occurred on. Determining seismicity rates for voxels on either side of the dike also risks separating secondary events from their "mainshocks." To avoid these complexities, we simply shifted the seismicity rates employed in the previous geometry (Figure 9) up into the next shallowest row of voxels. For the single row of deep voxels, the seismicity rate is divided evenly between the two rows of voxels in the next level up, so that each voxel on either side of the dike has the same number of events in each time step. The deepest row of voxels is now removed from the objective, as the deep dike model posits that this volume does not exhibit seismicity.

[53] For the results shown here the seismicity residuals are weighted 10 times GPS residuals, while the weighting on the time of peak seismicity is ~ 13 times the GPS residuals and smoothing of the pressure history (κ_2) is ~ 250 times the GPS residuals. As expected, we find that with this geometry it is possible to fit the rapid decay in seismicity without requiring extremely small t_a and attendant unreasonably large background stressing rates. For the case shown here $\dot{s}_r \simeq 9.9 \times 10^{-5}$ MPa/h corresponding to 0.87 MPa/yr. While this was the upper bound, for this parameter the
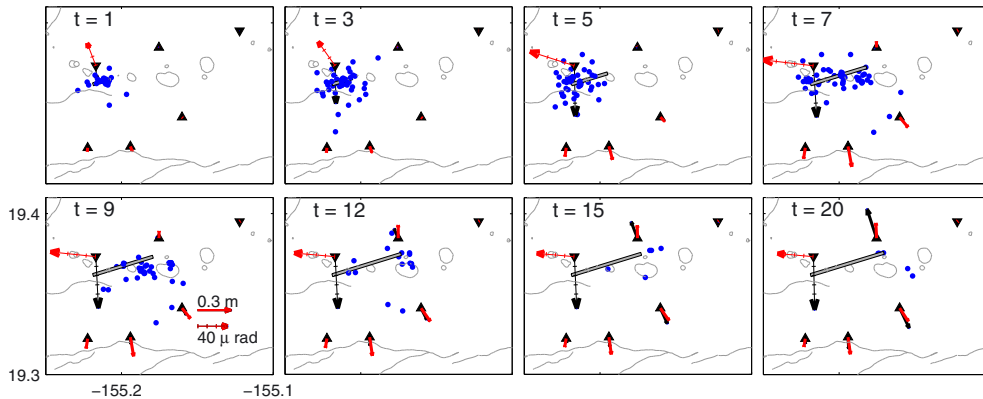
Figure 19. Father's Day inversion results including seismicity and deformation data, "Deep Dike" model. Map view of dike and predicted displacements and tilts (barbed) for inversion including seismicity data. Observed (black) and predicted (red) GPS displacements and tilts. Blue dots represent earthquake epicenters during the preceding 3 h.

Figure 20. Father's Day inversion results including seismicity and deformation data, "Deep Dike" model. Fit to north component of GPS displacement. Blue circles, observed with 2σ error bars; black, predicted.

bound is physically motivated and qualitatively good fits are obtained at or below the bound. (Restarting the optimization with a higher bound led to a very slight improvement in fit, with $\dot{s}_r \sim 4.7 \times 10^{-4}$.) The friction parameter a is 0.015 so that $a\sigma = 0.73$ MPa and $t_a \simeq 0.5$ years.

[54] In this model (Figures 15c and 15d) the dike grows very rapidly in the first 6 h, then slows slightly from 6 to 10 h, and then grows much more slowly after that, with a final growth spurt after 35 h. During the initial rapid elongation the dike excess pressure drops from 14 MPa to about 7 MPa. The model does fit the seismicity data quite well (Figure 18). In map view the dike tracks the extent of seismicity (Figure 19) and the space-time evolution of the dike matches the fast down-rift extension of the swarm (Figure 17, right). However, as with the shallower dike model (section 4.4), the predicted displacements occur earlier than observed by GPS (Figure 20).

5. Discussion

[55] Neither the shallow nor deep dike models fit both the seismicity and the GPS data simultaneously. A model fitting the deformation data alone lags the down-rift extent of seismicity (Figures 13 and 17, left). Models strongly weighting the seismicity predict deformation before it is observed in the GPS data (Figure 20). This implies that the geometric model of a purely laterally propagating dike with a vertical tip line is too simple. One possibility is that the leading edge of the dike is not vertical but sloping such that seismicity at depth is triggered prior to the dike opening nearer to the surface (Figure 21a). The GPS displacements, which are most sensitive to the depth averaged opening, thus lag the seismicity. In this interpretation the rapid down-rift expansion of seismicity ~ 5 h after the swarm onset reflects an apparent horizontal velocity of the dike. Another possibility is that the growth of the second en echelon segment involved significant vertical propagation (Figure 21b). This would imply that the segmentation extends to (at least near) seismogenic

depths. While the earthquake locations do not support this directly, it is possible the precision of the relative locations is inadequate to detect the segment separation at depth.

[56] *Dieterich et al.* [2003] propose that dike intrusion results from upward propagation of the deep rift body to the surface. In this case the deformation and stress changes accompanying the intrusion result from dilatation of the entire rift zone, not simply the upper ~ 3 km as in the case of shallow intrusion into an elastic half-space. They note that such a model requires smaller excess pressure, compatible with the magmastatic head, to dilate the dike sufficiently to fit geodetic data. Furthermore, the predicted stress changes are more compatible with the observed increase in decollement seismicity in the 90 days following the 1983 intrusion.

[57] In contrast, we analyze shallow East Rift Zone seismicity during the 48 h long Father's Day intrusion. These earthquakes are located within the ERZ, well above the decollement, and exhibit predominantly strike-slip mechanisms. On the time scale of the intrusion the evidence for lateral propagation is clear; seismicity and deformation both propagate down-rift [e.g., *Montgomery-Brown et al.*, 2011]. Furthermore, the first sign of intrusion is typically deflation at Kilauea summit, indicating that at least the early magma feeding the dike moves laterally from the summit. It is plausible, however, that longer term relaxation of dike-induced stress changes are consistent with equilibration of magma pressure over the full depth extent of the ERZ, as suggested by *Dieterich et al.* [2003]. This is supported by geodetic transients following some intrusions on Kilauea, including
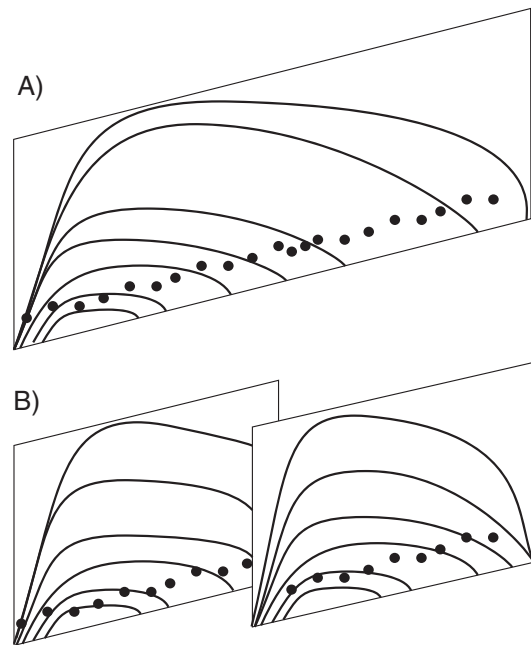
Figure 21. Possible explanations for seismicity leading the geodetically inferred dike. Curves mark isochrons showing position of dike-tip line. Dots mark earthquakes. (a) Dike opening at depth triggers seismicity prior to shallower opening sensed geodetically. (b) Two en echelon dike segments, each with significant component of vertical propagation. In both cases the dike emanates from an underlying conduit or deep rift body.

16

the 1997 Napau eruption, that are best explained by delayed rift opening below a shallow dike intrusion [*Desmarais and Segall*, 2007].

[58] If the intrusion-induced seismicity is dominantly triggered by the laterally propagating dike tip, then the localized depth extent of earthquakes is controlled by the depth dependence of the background stressing generated by continuous deep rift opening. A pronounced stress concentration near the top of the deep rift body is consistent with the narrow depth extent of background seismicity [*Gillard et al.*, 1996]. This stress concentration may also control where individual dikes nucleate. Dikes could also nucleate from the conduit feeding the Pu'u 'Ō'ō vent—it is presently unknown whether the conduit coincides with the top of the deep rift body. In either case, the preexisting conduit provides a pathway for magma from the summit magma reservoir into the dike. Subsidence of the crater floor at Pu'u 'Ō'ō during the eruption [*Poland et al.*, 2008; *Montgomery-Brown et al.*, 2010] also indicates that magma flowed from Pu'u 'Ō'ō into the dike. During intrusions the stress concentration at the leading dike edge adds to the highly localized background stress. This suggests that seismicity occurs at the bottom of the brittle region, where the background stressing is highest. Since seismicity rate during intrusions is proportional to the background rate (see equation (3)), it is expected that background and swarm earthquakes are concentrated at the same depth.

[59] Yet another possible explanation for the rapid decay in seismicity during the intrusion would be that the seismicity is originally located beneath the dike ("shallow dike model"), but the dike rapidly deepens dropping the seismically active volume into a stress shadow. This seems less likely if dikes nucleate in the stress concentration at the top of the deep rift body, although this effect could occur locally along strike as the dike propagates down-rift.

[60] The model fit to deformation data alone results in dike pressure increasing with time (Figure 12), whereas the deep dike model weighted to fit seismicity exhibits decreasing dike pressure (Figure 15). The latter is more in accord with expectation, since dike growth increases the net volume of the magmatic system and without addition of new magma must result in a pressure drop [e.g., *Segall et al.*, 2001].

[61] We have ignored thermal and thermo-poro-elastic stressing, as this is unlikely to be important on the time scale of dike propagation [*Rubin and Gillard*, 1998]. A dike traverses a region of spatial extent D in time D/v. For propagation speeds v of order 0.1 km/h or 3 cm/s and earthquake sources on the scale of 300 m, this corresponds to times of order 10^4 s. Thermal diffusivity of rock is of the order of $c = 10^{-6}$ m²/s, which leads to thermal penetration distances $L = \sqrt{ct}$ of order 10^{-1} m. Similarly, pore-pressure increases due to heating are only significant when the hydraulic diffusivity is small, and in these cases the penetration distances on the time scale of dike propagation are insignificant.

[62] The analysis also neglected the presence of a dike-tip cavity which is filled with either pore fluids from the surrounding rock or exsolved fluids from the magma. These fluids exist at $\Delta p < 0$ and permit the dike to close smoothly without stress singularity [*Rubin*, 1995]. The stresses computed from a uniformly pressurized crack are only accurate if the dike-tip cavity is small relative to the distance of the earthquakes from the dike. The length scale of the dike-tip

region depends on the degree of under pressure within the tip, which is not well known. Depending on the proximity of earthquakes to the dike, neglecting the dike-tip cavity may result in overestimating the dike-induced stress change. This is mitigated to some extent by the fact that we compute the stress at voxel centers some distance from the dike plane. Biases in the computed stress are likely to bias the background stressing rate and friction parameter a.

[63] The depth dependence of excess dike pressure also varies due to crustal density variations and depth dependent rheology. It is believed that bladelike dikes are trapped by zones of positive excess pressure, such that Δp decreases toward both the top and bottom of the dike. (These dike-trapping stresses are associated with what is commonly referred to as the "level of neutral buoyancy" [*Rubin*, 1995].) We examined the effect of depth-dependent pressure on the time-dependent inversion assuming a bilinear distribution of excess dike pressure with depth, $\Delta p(z) = p_0 - p'|z - z_c|$, where p_0 is the pressure at the dike center (depth z_c) and p' is the vertical pressure gradient. Choosing the gradient in pressure such that the stress intensity factors vanish at the upper and lower edges (according to a plane-strain calculation) requires $p' = \pi p_0/h$, where h is dike height [*Fialko and Rubin*, 1999, equation (3)]. At the dike top and bottom the excess pressure is negative (under pressure), $\Delta p = -p_0(\pi - 2)/2$.

[64] With the bilinear pressure distribution the average excess pressure is reduced by a factor of 1.14/4 relative to the uniformly pressurized dike. Thus, either the peak pressure has to be increased by a factor of ~ 4 relative to the uniform case (for the same dike height) or the shear modulus has to be reduced by a factor of ~ 4 to achieve an equivalent fit to the GPS displacements. GPS stations close to the rift zone are sensitive to the reduced shallow opening with the bilinear pressure distribution. We found that bringing the dike top to 100 m below the surface provides a reasonable fit to the data at NUPM.

[65] The rate of stressing computed at a voxel center can be much more than a factor of 4 less than computed in the uniform pressure case, depending on distance from the dike edge to the voxel center. (The stress, unlike displacement, does not scale with shear modulus given a pressure boundary condition.) With nonuniform pressure the stress distribution changes (in particular, the stress shadow is eliminated immediately above the dike bottom), so the stress-rate history is not simply a scaled version of the uniform pressure case. However, if the earthquakes are located below the dike bottom, the stress histories for the two pressure distributions are close to scaled versions of one another. In this case, scaling $\dot{s}_r$ and $a\sigma$ by the ratio of the bilinear to uniform stressing rates should leave the predicted seismicity rate relatively unchanged.

[66] We tested this with the "shallow dike" model, taking the solution described in the paper as a starting model but changing the pressure distribution to be bilinear, reducing the shear modulus by a factor of 4, and reducing the previous estimates of $\dot{s}_r$ and $a\sigma$ by factors of 10. The resulting dike model is qualitatively similar to previous estimates, although somewhat different in detail. The peak excess pressure (at the dike center) drops from ~ 7.5 MPa to ~ 5 MPa as the dike evolves. The predicted displacements lead the observations, as observed in other such models when the seismicity

data is heavily weighted in the objective. The background stressing rate is decreased to on the order of 2 MPa/yr; however, $a\sigma$ is also reduced in order to maintain t_a to ~ 8 days. Starting with an initial model much farther from the final estimate resulted in a similar but not identical result. For the deep dike model the stress driving strike-slip faulting adjacent to the dike depends strongly on depth. Future inversions will need to average over depth within voxels (rather than evaluate only at voxel centers) to properly compare predictions with observed seismicity.

[67] The deep dike model posits that the dike bottom extended at least somewhat below the brittle-ductile transition for earthquakes. This suggests that dike-trapping stresses and hence the "level of neutral buoyancy" is strongly influenced by the brittle-ductile transition in combination with south flank motion, as opposed to simply density stratification. This inference is consistent with the observation that the 2–3 km depth of diking [e.g., *Owen et al.*, 2000a; *Cervelli et al.*, 2002; *Montgomery-Brown et al.*, 2010] is indistinguishable from the top of the deep rift body [e.g., *Delaney et al.*, 1990; *Owen et al.*, 2000b].

[68] Estimates of the friction parameter a are conditional on the effective normal stress acting on the earthquake sources σ being lithostatic less hydrostatic pore pressure. In addition to uncertainties in pore pressure, the total stress acting on strike-slip faults is likely to be less than lithostatic. Assume that the intermediate principal stress is vertical (lithostatic). The minimum compressive stress (rift normal) can be no less than some fraction ϵ (roughly 0.3) of the vertical stress without normal faulting occurring within the rift zone [*Segall et al.*, 2001]. The oblique focal mechanisms suggest that the maximum compression is not much greater than the vertical stress. Taking this limit, the ratio of average horizontal stress to vertical stress is $(1+\epsilon)/2$. From a Mohr's circle construction, the ratio of σ acting on faults at failure to the average horizontal stress is $1/(1+f^2)$, where f is the friction coefficient. Thus, the ratio of σ to vertical stress is $(1+\epsilon)/2(1+f^2)$, which for $\epsilon \sim 0.3$ and $f \sim 0.6$ is of the order 0.5. This is almost certainly not the greatest source of uncertainty in the estimates of a.

[69] The absence of source interactions in the *Dieterich* [1994] theory is a significant limitation in applying the model to swarm sequences which contain secondary events. Attempts at declustering the earthquake catalog failed because they removed nearly all of the events. It is possible that an appropriate declustering algorithm would be useful. Another option would be to include an ETAS-like [*Ogata*, 1998] term in the forward model, perhaps allowing the largest events in the sequence to produce a cascade of secondary events. Of course a better solution would be to develop a physical model that predicts secondary events; however, this requires predicting the ultimate size of an earthquake once initiated, which is currently out of reach of analytical models.

6. Conclusion

[70] We have developed methods for the forward modeling and inversion of seismicity and deformation accompanying dike intrusion, assuming volcano-tectonic events resulting from shear failure of rock near the dike. For simplicity we currently model lateral propagation only and

estimate the dike length and overpressure at each time step. Forward models show that when seismicity is at intermediate depth between the dike top and bottom, earthquakes initiate near the leading edge of the dike, but seismicity cuts off as the dike tip passes and the seismogenic volume falls into a stress shadow. The crust off the dike ends, however, experiences more earthquakes as these volumes undergo positive stressing for a greater length of time. On the other hand, if quakes occur above or below the dike, seismicity is predicted to continue at a decaying rate after the dike tip passes. Both space-time patterns have been observed in nature.

[71] We apply the inversion approach to the 2007 Father's Day intrusion in Kilauea Volcano, Hawaii. Swarm seismicity during the intrusion propagated down-rift to the east, is localized in a narrow depth range at ~ 3 km, comparable to geodetic estimates of the dike bottom, and decays rapidly with time. We find that with lateral propagation and a vertical tip line it is difficult to fit both GPS data and the rapid down-rift jump in seismicity. This suggests significant vertical propagation during the intrusion, such that the rapid down-rift expansion of the swarm reflects an apparent velocity of dike propagation. One possibility is that each of the two en echelon dike segments inferred from steaming ground fractures and kinematic modeling of InSAR, GPS, and tilt data extend to significant depth. Vertical propagation of the second segment could then account for the rapid down-rift jump in seismicity.

[72] We explore both a "shallow" dike model, in which the seismicity is concentrated below the bottom edge of the dike, and a "deep dike" model, in which the dike extends below the seismicity. In the context of the deep model, the rapid decay in seismicity results from passage of the dike tip and seismicity falling into a stress shadow. In contrast, in the shallow dike model the rapid decay in seismicity rate following the passage of the dike tip requires a very short aftershock decay time and hence an unrealistically high background stressing rate. The deep dike model thus seems more consistent with the observations. However, if background stressing and seismicity rates are uniform along strike in Kilauea's East Rift Zone, the deep dike model predicts a strong concentration of seismicity at the eastern end of the intrusion, which is not observed. This apparent discrepancy could be explained if the 2007 dike ended in a volume of rock de-stressed by the 1999 Napau intrusion and eruption.

Appendix A: Omori Limit of Seismicity Equations

[73] We consider the following case: start at background stressing rate $\dot{s}_r$ and state $\gamma_0 = 1/\dot{s}_r$. Step 1, for a short period of length Δt, increase the stressing rate to $\dot{s} \gg \dot{s}_r$. This models rapid stressing during the intrusion. Step 2, return to stressing rate $\dot{s}_r$. For step 1, equation (8), in the limit $\dot{s}_r/\dot{s} \ll 1$, reduces to

$$\frac{R_1}{r} \simeq \exp\left(\frac{-\dot{s}\Delta t}{a\sigma}\right) = \exp\left(\frac{-\Delta s}{a\sigma}\right). \tag{A1}$$

At the same time, γ evolves from (7) to

$$\gamma_1 \simeq \frac{1}{\dot{s}_r} \exp\left(\frac{-\Delta s}{a\sigma}\right). \tag{A2}$$

[74] For step 2, the state starts at γ_1 and again evolves according to equation (8). This yields

$$\frac{R}{r} \simeq \frac{1}{(e^{-\Delta s/a\sigma} - 1)e^{-t/t_a} + 1}. \tag{A3}$$

The above is equivalent to *Dieterich* [1994] equation (12) when the stressing rate following the event returns to the background rate. For short times following the intrusion, $t/t_a \ll 1$, including the leading order terms in a Taylor series expansion of the exponential term, equation (A3) reduces to

$$\frac{R}{r} \simeq \frac{1}{e^{-\Delta s/a\sigma} + \frac{t}{t_a}}, \tag{A4}$$

which is of the form of Omori's law.

Appendix B: Implementation Details

B1. Forward Calculations

[75] It is important to ensure that the piecewise linear discretization of the stress is accurate. To that end if the stress rate in any voxel exceeds a predefined threshold, the time step is divided into uniform length substeps. The dike length L is linearly interpolated through the substeps, while the magma pressure history is estimated by cubic interpolation. The stress rate is computed from the derivative of a cubic spline fit to the stress computed at the substeps. Testing showed that this resulted in a smooth stress-rate history. Examples can be seen in Figure 16.

[76] Care also needs to be given to equations (7) through (9) in cases where $|\dot{s}_k \Delta t_k / a\sigma| \gg 1$. Equation (7) in the limit of $\dot{s}_k \Delta t_k / a\sigma \ll 0$ can lead to overflow, corresponding to $\gamma \to \infty$ and $R \to 0$. This is not a problem for a single dike intrusion; however, it should be noted that once an overflow condition occurs the seismicity rate can never be nonzero, even if the stress rate at a later time becomes positive. If $\dot{s}_k \Delta t_k / a\sigma \gg 1$ but $\gamma_{k-1}\dot{s}_k$ is finite, then (9) and (10) lead to $N \simeq rt_a (\dot{s}_k \Delta t_k / a\sigma - \ln \gamma_{k-1}\dot{s}_k)$. If, on the other hand, $\gamma_{k-1}\dot{s}_k$ is unbounded, this implies that $\gamma_k \dot{s}_k$ was unbounded at the beginning of the current time step because γ is continuous. Since $\dot{s}_k$ is finite, this implies γ_k is unbounded and the seismicity rate is set to $R = 0$.

[77] To accelerate the forward computations, we limit the number of function calls required to construct A in equation (1). Because the top and bottom edges of the dike parallel to the free surface and the dike grid elements are of equal length, stress interaction terms at a given depth are invariant to horizontal translation. Thus, we need to calculate Green's functions for only one element at each depth in the dike grid.

B2. Inversion

[78] The most computationally intensive aspect of the nonlinear optimization is the finite difference calculation of the Jacobian, $\partial\mathbf{r}/\partial\mathbf{m}$, where $\mathbf{r}$ are the weighted residuals whose sum of squares form the objective function (11), and the derivatives are evaluated at the current model estimate $\mathbf{m}$.

[79] Considering the structure of the Jacobian minimizes the number of calls to the computationally expensive elastic dislocation routines. First, examine the derivatives with respect to dike pressure,

$$\frac{\partial\mathbf{r}}{\partial\Delta p_k} = \frac{\partial\mathbf{r}}{\partial u}\frac{\partial u}{\partial\Delta p_k} + \frac{\partial\mathbf{r}}{\partial\dot{s}}\frac{\partial\dot{s}}{\partial s}\frac{\partial s}{\partial\Delta p_k}. \tag{B1}$$

The first term on the right relates to the GPS residuals (tilt is analogous). Notice that the displacements are linear in the pressure Δp so that a single elastic dislocation calculation is sufficient to compute $\partial u/\partial\Delta p_k$ for fixed dike length L_k. The second term relates to the seismicity-rate residuals. The first matrix here $\partial\mathbf{r}/\partial\dot{s}$ gives the dependence of the seismicity rate on stress rate (for example by differentiating (8)), while the second represents the finite difference computation of stress rate. The stress due to the dike, $\partial s/\partial\Delta p_k$, is again linear in pressure so that only the single call to the dislocation routine is required.

[80] Next, consider the derivatives with respect to dike length

$$\frac{\partial\mathbf{r}}{\partial\Delta L_k} = \frac{\partial\mathbf{r}}{\partial u}\frac{\partial u}{\partial\Delta L_k} + \frac{\partial\mathbf{r}}{\partial\dot{s}}\frac{\partial\dot{s}}{\partial s}\frac{\partial s}{\partial\Delta L_k}. \tag{B2}$$

The stress and deformation depend only on the total dike length $L_k = \sum_{j=1}^{k} \Delta L_j$. Thus, for example, $\partial u/\partial\Delta L_j = \partial u/\partial L_k$ for all $j \leq k$ and is zero otherwise. The same relation holds for the derivatives of the stress. Thus, while we calculate each of the columns of the Jacobian using finite differences, we use the above relationships to reduce the number of calls to the dislocation routines; for deformation residuals this is equal to the number of time epochs, and for seismicity the fine time stepping requires more calls. In practice the cost of computing the Jacobian is roughly 2.5 to 3 times the cost of a single forward calculation of displacement and stress change.

Appendix C: Focal Mechanisms

[81] Due to seemingly erroneous first motions at some stations, the polarities of the vertical components at all HVO and SEQ stations recording during the Father's Day intrusion were checked. The unfiltered waveforms for a total of 10 teleseismic events were compared to identify stations with polarities that were reversed between April and July 2007. The polarities of HVO stations DES, HPU, HSS, and WOO were reversed during this time period, and station PAU may have been reversed, although support of a polarity reversal is less clear at this station. Due to the uncertainty for station PAU, its polarities were omitted from the focal mechanism calculations, and the polarity picks for the other four stations with identified reversals were corrected prior to calculation. While we can identify which stations had reversed polarities during this time period, we made no attempt to assess the reversals before or after this period of interest. No polarity problems were identified with the temporary SEQ stations.

References

Belachew, M., C. Ebinger, D. Coté, D. Keir, J. Rowland, J. Hammond, and A. Ayele (2011), Comparison of dike intrusions in an incipient seafloor-spreading segment in Afar, Ethiopia: Seismicity perspectives, *J. Geophys. Res.*, *116*(B6), B06405, doi:10.1029/2010JB007908.

Brandsdottir, B., and P. Einarsson (1979), Seismic activity associated with the September 1977 deflation of the Krafla central volcano in northern Iceland, *J. Volcanol. Geoth. Res.*, *6*, 197–212.

Cervelli, P., P. Segall, F. Amelung, H. Garbeil, C. Meertens, S. Owen, A. Miklius, and M. Lisowski (2002), The 12 September 1999 upper east rift zone dike intrusion at Kilauea volcano, Hawaii, *J. Geophys. Res.*, *107* (B7), 2150, doi:10.1029/2001JB000602.

Coleman, T., and Y. Li (1996), An interior trust region approach for nonlinear minimization subject to bounds, *SIAM J. Optim.*, *6*(2), 418–445.

Delaney, P., R. Fiske, A. Miklius, A. Okamura, and M. Sako (1990), Deep magma body beneath the summit and rift zones of Kilauea volcano, Hawaii, *Science*, *247*(4948), 1311–1316.

Desmarais, E. K., and P. Segall (2007), Transient deformation following the 30 January 1997 dike intrusion at Kīlauea volcano, Hawaii, *Bull. Volcanol.*, *69*(4), 353–363.

Dieterich, J. (1994), A constitutive law for rate of earthquake production and its application to earthquake clustering, *J. Geophys. Res.*, *99*(B2), 2601–2618.

Dieterich, J., V. Cayol, and P. Okubo (2000), The use of earthquake rate changes as a stress meter at Kilauea volcano, *Nature*, *408*(6811), 457–460.

Dieterich, J. H., V. Cayol, and P. Okubo (2003), Stress changes before and during the Pu'u O'o-Kupaianaha eruptions, *U.S. Geol. Surv. Prof. Pap.*, *1676*, 187–202.

Ebinger, C., A. Ayele, D. Keir, J. Rowland, G. Yirgu, T. Wright, M. Belachew, and I. Hamling (2010), Length and timescales of rift faulting and magma intrusion: The Afar rifting cycle from 2005 to present, *Ann. Rev. Earth Planet. Sci.*, *38*(1), 439–466.

Fialko, Y. A., and A. M. Rubin (1999), What controls the along-strike slopes of volcanic rift zones?, *J. Geophys. Res.*, *104*(B9), 20,007–20,020.

Gillard, D., A. M. Rubin, and P. Okubo (1996), Highly concentrated seismicity caused by deformation of Kilauea's deep magma systems, *Nature*, *384*(6607), 343–346.

Grandin, R., E. Jacques, A. Nercessian, A. Ayele, C. Doubre, A. Socquet, D. Keir, M. Kassim, A. Lemarchand, and G. King (2011), Seismicity during lateral dike propagation: Insights from new data in the recent Manda Hararo–Dabbahu rifting episode (Afar, Ethiopia), *Geochem. Geophys. Geosyst.*, *12*, Q0AB08, doi:10.1029/2010GC003434.

Hardebeck, J., and P. Shearer (2002), A new method for determining first-motion focal mechanisms, *Bull. Seismol. Soc. Am.*, *92*(6), 2264–2276.

Klein, F., Y. Koyanagi, J. Nakata, and W. Tanigawa (1987), The seismicity of Kilauea's magma system, *U.S. Geol. Surv. Prof. Pap.*, *1350*, 1019–1185.

Larsen, G., and K. Grönvold (1979), Volcanic eruption through a geothermal borehole at Namafjall, Iceland, *Nature*, *278*, 707–710.

Linker, M. F., and J. H. Dieterich (1992), Effects of variable normal stress on rock friction: Observations and constitutive equations, *J. Geophys. Res.*, *97*(B4), 4923–4940.

Llenos, A., P. Segall, C. Thurber, and E. Syracuse (2010), Time-dependent imaging of dike propagation from deformation and seismicity data: Application to the 2007 Kilauea intrusion, *EOS Trans. AGU*, *91*(26), abstract V31E-08.

Llenos, A., P. Segall, C. Thurber, E. Syracuse, and D. Peterson (2011), Modeling time-dependent dike propagation during the 2007 Father's day intrusion from seismicity and deformation data, *EOS Trans. AGU*, *91*(26), abstract V22A-06.

Llenos, A. L., and J. J. McGuire (2011), Detecting aseismic strain transients from seismicity data, *J. Geophys. Res.*, *116*, B06305, doi:10.1029/2010JB007537.

Montgomery-Brown, E., D. Sinnett, M. Poland, P. Segall, T. Orr, H. Zebker, and A. Miklius (2010), Geodetic evidence for en echelon dike emplacement and concurrent slow slip during the june 2007 intrusion and eruption at Kīlauea volcano, Hawaii, *J. Geophys. Res*, *115*, B07405, doi:10.1029/2009JB006658.

Montgomery-Brown, E., D. Sinnett, K. Larson, M. Poland, P. Segall, and A. Miklius (2011), Spatiotemporal evolution of dike opening and décollement slip at Kīlauea volcano, Hawaii, *J. Geophys. Res*, *116*, B03401, doi:10.1029/2010JB007762.

Ogata, Y. (1998), Space-time point-process models for earthquake occurrences, *Ann. Inst. Statist. Math.*, *50*(2), 379–402.

Okada, Y. (1992), Internal deformation due to shear and tensile faults in a half-space, *Bull. Seism. Soc. Am.*, *82*, 1018–1040.

Okamura, A., J. J. Dvorak, R. Koyanagi, and W. Tanigawa (1988), Surface deformation during dike propagation, in *The Pu'u O'o Eruption of Kilauea Hawaii: Episodes 1 Through 20, January 3, 1983 Through June 8, 1984,* vol. 1463, edited by E. Wolfe, pp. 165–182, US Geological Survey Professional Paper, Washington, D.C.

Owen, S., P. Segall, M. Lisowski, A. Miklius, M. Murray, M. Bevis, and J. Foster (2000a), January 30, 1997 eruptive event on Kilauea volcano, Hawaii, as monitored by continuous GPS, *Geophys. Res. Lett.*, *27*(17), 2757–2760.

Owen, S., P. Segall, M. Lisowski, A. Miklius, R. Denlinger, and M. Sako (2000b), Rapid deformation of Kilauea volcano: Global positioning system measurements between 1990 and 1996, *J. Geophys. Res.*, *105*(B8), 18,983–18,998.

Poland, M., A. Miklius, T. Orr, J. Sutton, C. Thornber, and D. Wilson (2008), New episodes of volcanism at Kilauea Volcano, Hawai'i, *EOS Trans. AGU*, *89*(5), 37–38.

Rubin, A. (1992), Dike-induced faulting and graben subsidence in volcanic rift zones, *J. Geophys. Res.*, *97*(B2), 1839–1858.

Rubin, A., and D. Gillard (1998), Dike-induced earthquakes: Theoretical considerations, *J. Geophys. Res.*, *103*(B5), 10,017–10,030, doi:10.1029/97JB03514.

Rubin, A. M. (1995), Propagation of magma-filled cracks, *Annu. Rev. Earth Planet. Sci.*, *23*, 287–336.

Rubin, A. M., D. Gillard, and J.-L. Got (1998), A reinterpretation of seismicity associated with the January 1983 dike intrusion at Kilauea volcano, Hawaii, *J. Geophys. Res.*, *103*, 10,003–10,015.

Segall, P., and S. H. Yun (2005), Imaging dike intrusion by joint inversion of deformation and seismicity, *Eos Trans. AGU*, *86*(52), abstract V14B-01.

Segall, P., P. Cervelli, S. Owen, M. Lisowski, and A. Miklius (2001), Constraints on dike propagation from continuous GPS measurements, *J. Geophys. Res.*, *106*(B9), 19,301–19,317.

Segall, P., E. K. Desmarais, D. Shelly, A. Miklius, and P. Cervelli (2006), Earthquakes triggered by silent slip events on Kilauea volcano, Hawaii, *Nature*, *442*, 71–74, doi:10.1038/nature04938.

Syracuse, E., C. Thurber, C. Wolfe, P. Okubo, J. Foster, and B. Brooks (2010), High-resolution locations of triggered earthquakes and tomographic imaging of Kilauea volcano's south flank, *J. Geophys. Res.*, *115*(B10), B10310, doi:10.1029/2010JB007554.

Toda, S., R. Stein, and T. Sagiya (2002), Evidence from the 2000 Izu islands earthquake swarm that stressing rate governs seismicity, *Nature*, *419*(6902), 58–61.

Wallace, M., and P. Delaney (1995), Deformation of Kilauea volcano during 1982 and 1983: A transition period, *J. Geophys. Res.*, *100*(B5), 8201–8219.

Yun, S., P. Segall, and H. Zebker (2006), Constraints on magma chamber geometry at Sierra Negra volcano, Galapagos islands, based on InSAR observations, *J. Volcanol. Geotherm. Res.*, *150*(1-3), 232–243.

Zhang, H., and C. Thurber (2003), Double-difference tomography: The method and its application to the Hayward fault, California, *Bull. Seismol. Soc. Am.*, *93*(5), 1875–1889.